Interfacial Disulfide Chemistry and Plasma Surface Activation for Fatigue Healing in Carbon Fiber / UHMWPE Composites

A Thesis Presented for the

Master of Science

Degree

The University of Tennessee, Knoxville

Chase McCullar

May 2026

Copyright © 2026 by Chase McCullar

All rights reserved.

ABSTRACT

Fiber-reinforced polymer laminates are widely used in aerospace, defense, and transportation industries for their high specific strength and stiffness. However, their stacked-ply construction produces resin-rich interlaminar regions that are inherently prone to delamination, regardless of whether the plies are nonwoven mats, unidirectional tapes, or woven fabrics. The main damage mode for these laminates is fatigue-driven delamination growth. Under cyclic loading, sub-critical delamination can propagate at energy release rates far below the static fracture toughness. These flaws accumulate with each cycle until catastrophic failure. Traditional repair methods address the symptoms of delamination rather than restoring the original interface. Self-healing composites have emerged to address this. However, these systems are either single-use, complex to manufacture, or rely on physical chain entanglement. Most of the published vitrimer composite systems distributes dynamic chemistry throughout the entire matrix rather than localizing it in the delamination prone interply region.

This work develops an interply healing composite in which 4-aminophenyl disulfide (4-APD) is applied as a standalone compound at the ply interfaces of a nonwoven carbon fiber/ultra-high molecular weight polyethylene (CF/UHMWPE) composite. Atmospheric plasma surface treatment is used to generate the polar functional groups required to anchor the 4-APD at those interfaces. Four variants were fabricated and tested: an untreated control (CN), plasma only (CP), 4-APD only (CD), and the combined variant (CPD). Each was characterized by Fourier Transform Infrared (FTIR) spectroscopy, water contact angle, three-point bend fatigue, X-ray computed tomography, three-point bend fatigue testing, and dynamic mechanical analysis.

After 30 minutes of fatigue and a healing cycle, CPD achieved a full-curve fatigue healing efficiency of 94.7%, exceeding all other variants with highly reproducible recovery

across specimens. X-ray CT was used to compute void content. CPD returned to within 3.2% of its original void content, while CN remained 18.8% above baseline. CN also exhibited the largest fatigue variance and had visible deformation post-heal. These results establish interfacial anchoring of dynamic covalent chemistry as a viable alternative to bulk vitrimer matrices for fatigue-healable thermoplastic composites.

TABLE OF CONTENTS

CHAPTER ONE – INTRODUCTION AND BACKGROUND INFORMATION 1

Fiber-Reinforced Polymer Composites 1

The Delamination Problem 4

Toward Healable Composites 9

Covalent Adaptable Networks 10

Sequence of Document 11

CHAPTER TWO – LITERATURE REVIEW 12

Healing Strategies for Fiber-Reinforced Composites 12

Covalent Adaptable Networks 16

Vitrimer Chemistry 16

Disulfide Exchange Chemistry and 4-APD 22

Carbon Fiber and UHMWPE 25

Plasma Surface Treatment of Carbon Fiber and UHMWPE 26

Summary and Research Gap 28

CHAPTER THREE – MATERIALS AND METHODS 30

Nonwoven Mat Fabrication 30

Composite Fabrication 32

4-Aminophenyl Disulfide 33

Plasma Surface Treatment 34

Three-Point Bend Fatigue Testing 40

X-Ray Computed Tomography 44

Dynamic Mechanical Analysis 46

Data Analysis and MATLAB Processing 48

CHAPTER 4 – RESULTS AND DISCUSSION 49

Fourier Transfer Infrared Spectroscopy 49

Water Contact Angle 51

Three-Point Bend Fatigue Test 55

X-Ray Computed Tomography 62

Dynamic Mechanical Analysis 66

CHAPTER FIVE – CONCLUSIONS AND RECOMMENDATIONS 70

Plasma Surface Treatment 70

Disulfide Interfacial Chemistry 71

The Combined CPD Variant 72

Recommendations for Future Work 72

Closing Remark 74

REFERENCES 75

VITA 100

LIST OF TABLES

Table 3.1 31

Table 3.2 37

Table 4.1 52

Table 4.2 60

Table 4.3 63

LIST OF FIGURES

Figure 1.1 2

Figure 1.2 3

Figure 1.3 6

Figure 3.1 31

Figure 3.2 34

Figure 3.3 35

Figure 3.4 38

Figure 3.5 42

Figure 3.6 45

Figure 3.7 47

Figure 4.1 50

Figure 4.2 50

Figure 4.3 53

Figure 4.4 56

Figure 4.5 57

Figure 4.6 59

Figure 4.7 64

Figure 4.8 65

Figure 4.9 67

CHAPTER ONE – INTRODUCTION AND BACKGROUND INFORMATION

Fiber-Reinforced Polymer Composites

Fiber-reinforced polymer composites have become indispensable structural materials in aerospace, defense, energy, and transportation applications where minimizing weight without sacrificing strength is a primary design objective. The Boeing 787 Dreamliner and Airbus A350 XWB derive more than half of their structural mass from composite materials [1], and the global composites market is projected to grow at a compound annual growth rate (CAGR) between 5% and 8% through the early 2030s as these materials penetrate new industrial sectors [2]. However, the structural efficiency of composite laminates is fundamentally compromised by their susceptibility to delamination, an internal damage mode that can reduce load-carrying capacity by forty percent (40%) or more while leaving the external surface virtually undamaged [3], [4]. Current practice addresses this vulnerability through conservative design allowables and mandatory inspection programs that significantly increase lifecycle costs [5].

Fiber-reinforced polymer (FRP) composites combine high-strength reinforcing fibers with a continuous polymer matrix, producing a material in which the reinforcement carries applied loads while the matrix transfers stress between fibers and provides environmental protection [6-9].

FRPs are particularly appealing in the industrial/structural sectors due to their high stiffness-to-weight ratios and extraordinary strength [10]. By weight, carbon fiber reinforced polymers (CFRPs) can achieve specific strength values 5 - 10 times greater than structural steel and 2 - 4 times greater than aerospace-grade aluminum alloys [11]. CFRPs achieve these astonishing results by the combination of low-density polymer matrices and high-performance fibers with mechanical properties far beyond those of any monolithic engineering material [12],

[13]. Material property selection charts developed by Ashby [13] demonstrate that CFRPs occupy a region of specific strength–specific stiffness space that is inaccessible to metals and ceramics. This performance envelope, combined with low density, establishes CFRPs as the premier structural material when weight is a primary design driver [13], [14] (see **Figure 1.1**).

Selecting an FRP composite for a given application requires consideration of four key variables: (1) reinforcement fiber type; (2) polymer matrix type, (3) fiber architecture, and (4) manufacturing method. The most widely used reinforcing fibers are carbon, glass, and aramid, with each offering a distinct combination of stiffness, strength, density, and cost [8], [15]. Polymer matrices are classified into two main categories: thermosets, which undergo irreversible chemical crosslinking to form permanent covalent networks [16], [17], and thermoplastics,

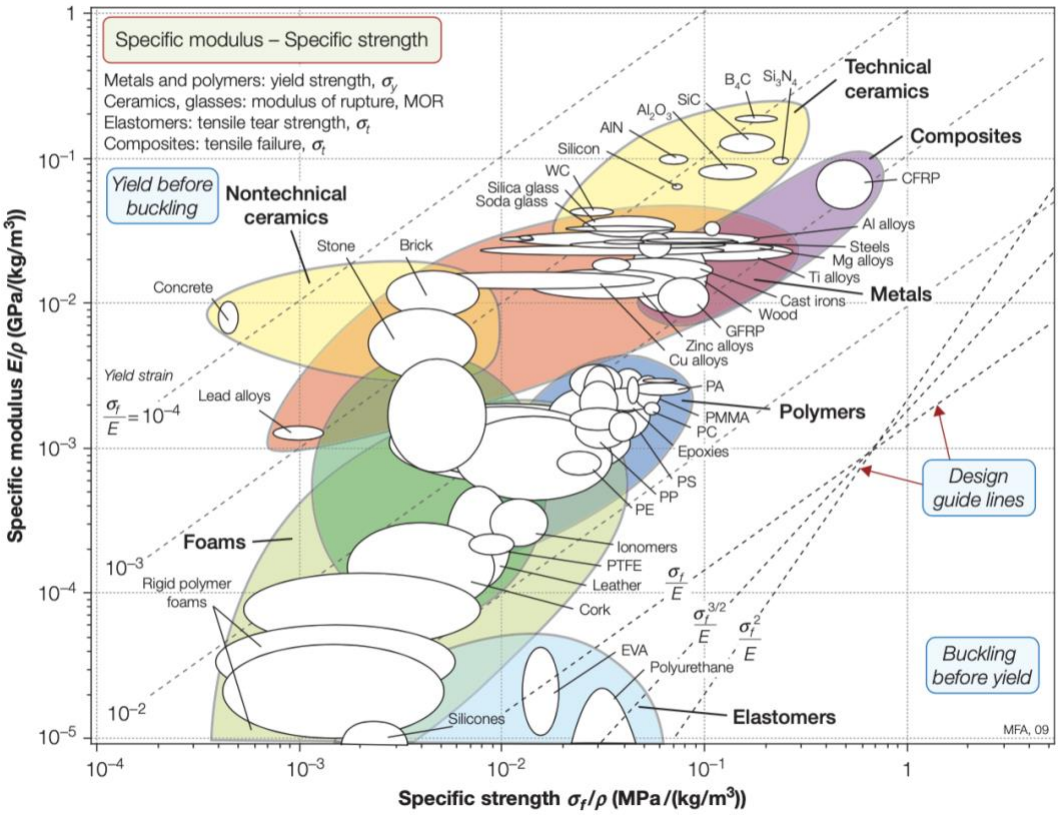


Figure 1.1. Ashby plot of specific modulus versus specific strength [18].

which consist of linear or branched chains held together by secondary physical interactions capable of softening, reshaping, and reprocessing [19], [20], [21]. The distinction between these two matrix classes is fundamental to this thesis. A thermoset matrix that has been crosslinked cannot reform broken covalent bonds, making damage permanent at the molecular level [22], [23]. A thermoplastic matrix, by contrast, can re-form chain entanglements across a damaged interface when heated, enabling fusion bonding and welding [24]. However, thermoplastic composites generally require higher processing temperatures and pressures, and their melt viscosities can create significant challenges for fiber impregnation [25]. The physical and molecular differences between thermosets and thermoplastics are shown in **Figure 1.2.**

Fiber architecture describes how fibers are arranged within the composite and can be manipulated to tailor directional mechanical properties [26]. Architectures range from

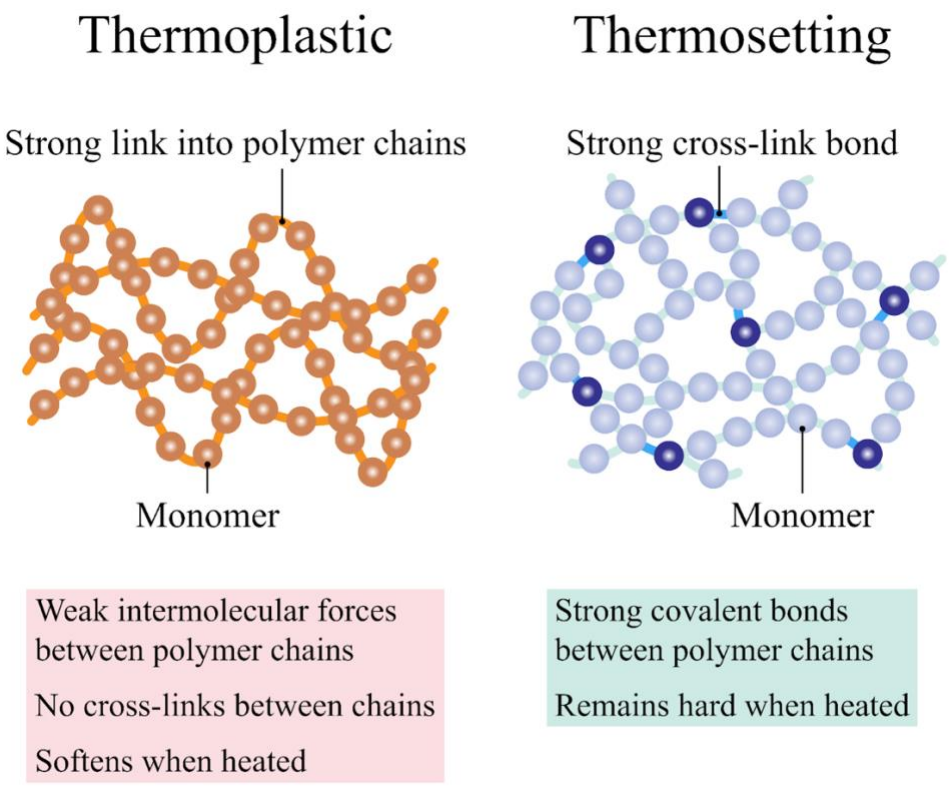


Figure 1.2. Physical and molecular differences between thermosets and thermoplastics [27].

unidirectional layups that maximize strength along a single axis [28], to woven fabrics that provide balanced in-plane properties [29], [30], to nonwoven mats in which fibers are randomly distributed within a plane [31]. Nonwoven mats are a popular architecture for thermoplastic composites because they facilitate matrix penetration during hot-press consolidation, a significant advantage when processing high-viscosity matrix materials such as ultra-high molecular weight polyethylene (UHMWPE) [32], [33]. The manufacturing method itself impacts mechanical properties, void content, fiber volume fraction, and surface quality [34], and is driven by matrix type, fiber architecture, part geometry, production volume, and cost constraints [35]. A detailed discussion of composite constituents and manufacturing methods is provided in Chapter Two.

The Delamination Problem

The stacked ply construction that gives composite laminates their design flexibility also introduces one of their most significant vulnerabilities. Stacked ply construction refers to the assembly of a laminate from discrete plies. These plies are typically made from nonwoven mats, unidirectional tapes, or woven fabrics. The plies are consolidated under heat and pressure to form a single structural part. Two distinct interfaces exist within a laminate: the fiber-matrix interface, and the interply (interlaminar) interface. The fiber–matrix interface governs local stress transfer between an individual reinforcing fiber and the surrounding polymer. The interply interface governs stress transfer between adjacent plies [36]. It is the interply interface that concerns the present work. In this region there are no reinforcing fibers that bridge the plane between two plies instead, it consists almost entirely of matrix polymer and any processing-related voids. It is therefore weaker than the fiber-dominated in-plane directions for three main reinforcing reasons. (1) The region carries no fibers to resist a propagating crack, so there is no bridging or pull-out

mechanism to dissipate fracture energy [37]. (2) The local strength is set by the polymer matrix and by fiber–matrix adhesion on the outer surfaces of each ply, both of which are much lower than the longitudinal fiber strength [36], [37]. (3) The mismatch in elastic properties between adjacent plies generates three-dimensional interlaminar stresses under in-plane loading that do not exist within a single ply [38], [39]. The separation of adjacent plies along this compliant plane is called delamination, and it is widely recognized as one of the most critical damage modes in composite structures [40], [41]. A schematic of a layered composite demonstrating the interply regions is shown in **Figure 1.3.**

Composite laminates are also susceptible to delamination from sources inherent to their design and manufacturing technique. At the free edges of a laminate, the mismatch in elastic properties between plies of different fiber orientations generates three-dimensional interlaminar stress fields that do not exist in the interior of the plate [38], [42]. These free-edge stresses can be sufficient to initiate delamination even under routine mechanical loading, particularly in laminates with large angles between adjacent ply orientations. Similarly, structural features such as fastener holes and cutouts create local stress concentrations that elevate interlaminar stresses in the surrounding material, providing preferential sites for delamination onset [43].

Manufacturing-induced defects, including foreign object inclusions, voids, and resin-starved regions, introduce additional weak points at the interlaminar interface that can serve as nucleation sites for delamination under subsequent loading [38]. Taken together, these mechanisms mean that delamination is not solely the result of accidental damage events but is an inherent vulnerability of the laminated architecture itself.

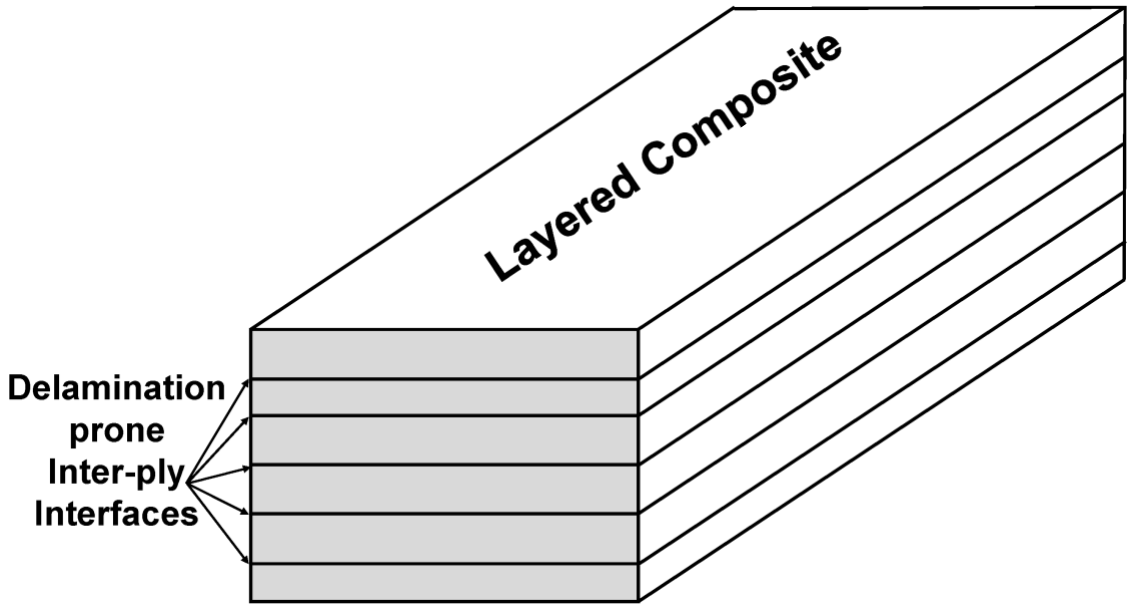


Figure 1.3. Layered composite schematic [44]

Once initiated, delamination propagates under continued loading in accordance with three modes of interlaminar fracture mechanics [45]. In Mode I, the crack faces separate normal to the crack plane. In Mode II, the crack faces slide relative to each other in the direction of crack propagation (sliding shear). In Mode III, the crack faces slide parallel to the crack front (tearing shear). While theoretically delamination can occur discretely in each mode, in practice, delamination growth typically occurs when Modes I and II combine to produce normal and sliding shears [38], [46].

The damage mode that dominates the lifecycle of most composite structures in service is fatigue-driven delamination growth. Aircraft fuselages experience pressurization cycles on every flight. Wind turbine blades endure 10^8 to 10^9 fatigue cycles over a twenty-year service life. Automotive suspension components are loaded with every road input. Under these cyclic loading conditions, delamination grows progressively at energy release rates far below the static fracture toughness, following a Paris-law relationship similar to fatigue crack growth in metals [47]. Asp et al. (2001) showed that a delamination which would remain stable under any individual load the structure is expected to encounter can grow incrementally with each cycle, accumulating damage until it reaches a critical size that triggers catastrophic failure [48]. The dangerous nature of this fatigue-driven growth is compounded by the difficulty of detecting subcritical delamination by visual inspection. The damage may remain entirely internal until the final failure event.

Current design practice attempts to address the delamination vulnerability through a damage tolerance philosophy whereby structures are designed to sustain a specified level of damage without catastrophic failure for a defined inspection interval [49]. This approach requires users to implement hypercautious safety thresholds that reduce the allowable strain levels to well

below the material's ultimate capability, hampering the structural efficiency of the composite in favor of structural conservatism. The economic cost of this conservatism is compounded by the expense of mandatory inspection programs using specialized nondestructive evaluation (NDE) techniques such as ultrasonic scanning, acoustic sensing, vibration analysis, thermography, and X-ray computed tomography [4].

Once delamination damage is detected, repair options are limited, and each carries its own significant constraints. Bonded scarf-patch repair is the industry standard for high-performance laminates because it restores the smooth outer mold-line geometry required in aerospace applications [50]. This method requires removal of the damaged material in a precisely tapered geometry, which is both time-consuming and dependent on the operator [50], [51]. This method also requires access to at least one free surface. For deeper repairs, access to both surfaces of the part is required. This is often impossible in closed-section components such as wing skins over integral stringers or fuel-tank walls [52]. This method typically uses pre-impregnated repair plies under vacuum and elevated temperature. The cure environment must also be heavily controlled to achieve consistent strength recovery. [53], [54]. Bolted double-lap repairs are quicker to execute and do not require a controlled cure, but they introduce stress concentrations at fastener holes and add additional weight [55]. Resin injection can be used to fill delamination sites with adhesive, but it cannot restore the original fiber–matrix interface on the crack faces and generally provides only limited structural recovery [56]. In all cases, conventional repair methodologies address the symptom of damage rather than restoring the material to its original microstructural state [57]. A composite material system capable of reversing delamination damage through a controlled healing process would fundamentally alter

this cost–safety tradeoff, reduce the burden of inspection, and extend the useful service life of composite structures.

Toward Healable Composites

The recognition that delamination is often difficult to detect, difficult to repair, and responsible for a significant fraction of composite lifecycle costs has driven substantial research into materials with embedded healing functionalities [57], [58]. Healing strategies for composites have progressed from capsule-based systems that release liquid monomers into crack planes [59], to vascular networks that deliver healing agents through refillable microchannels [60], [61], to thermoplastic interleaf approaches that place meltable films between plies to flow into delamination cracks upon heating [62], [63], [64], [65]. .

Each of these strategies carries fundamental limitations. Capsule-based systems are single-use: once the capsules along a given crack path have been ruptured, no further healing is possible at that location [58]. Vascular networks enable repeated healing but require complex channel fabrication and are susceptible to blockage [60]. Thermoplastic interleaf healing has shown the most promising combination of repeatability and simplicity, but the bonds it forms during healing are physical in nature, relying on chain interdiffusion and entanglement across the crack plane rather than on the reformation of covalent bonds [65], [66]. Because physical entanglements lack the defined bond energies of covalent linkages, their strength scales with the extent of interdiffusion achieved during the thermal cycle and is sensitive to local processing conditions, chain mobility, and cooling rate. The resulting healed strength is inherently less predictable and, on average, lower than that of the original covalent network it is attempting to restore [65].

An alternative strategy is to replace the physical entanglement mechanism altogether with a chemical mechanism in which the covalent bonds that were broken by damage are reformed across the crack plane. This is the defining feature of a class of polymer networks known as covalent adaptable networks.

Covalent Adaptable Networks

A class of polymer networks known as covalent adaptable networks (CANs) offers the possibility of combining the mechanical strength of covalent crosslinks with the reprocessability and healability of thermoplastics [67]. Within this class, vitrimers are associative CANs in which bond exchange reactions maintain a constant crosslink density at all temperatures, preserving dimensional stability while enabling topology rearrangement above an activation temperature [68]. Among the many exchange chemistries explored in vitrimer networks, disulfide exchange has attracted particular attention because it requires no external catalyst, eliminating the practical concerns of catalyst cost, leaching, and deactivation [69], [70], [71]. The compound 4-aminophenyl disulfide (4-APD) is uniquely suited to this application because it provides both reactive amine groups for covalent bonding and a central disulfide bridge for dynamic exchange [72], [73]. These topics are reviewed comprehensively in Chapter Two.

However, every published vitrimer composite system to date places the dynamic disulfide bonds throughout the entire polymer matrix rather than selectively at the interlaminar interfaces where delamination initiates and propagates. Furthermore, both carbon fiber and UHMWPE present inherently inert surfaces that resist bonding [74], [75], [76]. Plasma surface treatment can overcome this inertness by generating oxygen-containing functional groups on the material's surface without altering its bulk properties [77], [78], providing the reactive sites necessary for the covalent attachment of 4-APD molecules. The combination of these three elements, neat 4-

APD as a standalone interply healing agent, atmospheric plasma surface activation as a covalent anchoring strategy, and the CF/UHMWPE nonwoven material system, has no precedent in the published literature.

Sequence of Document

The remainder of this thesis is organized as follows: Chapter Two reviews the scientific literature on composite healing strategies, vitrimer chemistry, disulfide exchange mechanisms, plasma surface activation, and the CF/UHMWPE material system. Chapter Three describes the materials, fabrication procedures, and experimental methods. Chapter Four presents the results and provides a mechanistic discussion of the experimental findings. Chapter Five summarizes the conclusions and offers recommendations for future work.

CHAPTER TWO – LITERATURE REVIEW

This chapter reviews the scientific literature relevant to the present work. This review is organized thematically, progressing from healing strategies for composite materials through vitrimer chemistry and disulfide exchange mechanisms, plasma surface activation of polymers and carbon fiber, and the carbon fiber/UHMWPE composite system. This chapter concludes with a synthesis of the literature identifying the specific research gaps addressed by this research.

Healing Strategies for Fiber-Reinforced Composites

Healing strategies for fiber-reinforced polymer composites have progressed rapidly since the initial ground-breaking work of White et al. in 2001 [79]. Three primary methodologies have emerged: (1) capsule-based healing; (2) vascular system healing; and (3) thermoplastic interleaf healing, with each offering unique trade-offs between healing efficiency, repeatability, and manufacturing complexity. [79] [80], [81], [82].

Capsule-based healing relies on encapsulated liquid healing agents dispersed throughout the matrix that are released when a propagating crack ruptures a capsule [79], [83], [84].

White et al. (2001) pioneered the concept of autonomic self-healing in structural polymers by embedding microencapsulated dicyclopentadiene (DCPD) healing agents and Grubbs' first-generation ruthenium catalysts within an epoxy matrix [79]. When cracks propagated through the material, they ruptured the urea-formaldehyde microcapsules, releasing the DCPD monomer into the crack plane via capillary action. Contact with the embedded catalyst triggered ring-opening metathesis polymerization (ROMP) at room temperature, forming a crosslinked poly(DCPD) network that bonded the crack faces. Fracture testing using tapered double-cantilever beam specimens demonstrated up to 75% recovery of virgin fracture toughness, with an average healing efficiency of 60% across independently prepared samples.

Notably, all three types of control samples showed no healing whatsoever, confirming that both components are necessary for the autonomous repair mechanism.

Jin et al. developed a dual-microcapsule self-healing system for thermoset epoxy that eliminated the need for transition-metal catalysts by separately encapsulating the two components of an epoxy-amine healing chemistry [85]. Epoxy microcapsules were prepared via in situ urea-formaldehyde polymerization, while amine microcapsules were produced through a novel approach of vacuum infiltrating modified aliphatic polyamine into hollow polymeric microcapsules. Upon crack damage, both capsule types ruptured and released their contents into the crack plane. The epoxy and amine then reacted to form a crosslinked polymer chemically compatible with the host matrix. At an optimal amine-to-epoxy capsule mass ratio of 4:6 and a total loading of 17.5 wt%, the system achieved an average healing efficiency of 91%. The system also demonstrated good long-term stability, retaining 68% healing efficiency after six months at ambient conditions, a significant improvement over solvent-based approaches that lost all healing capacity within eight months. However, thermal stability remained a limitation, as post-curing at 121°C caused amine leakage from the capsules and reduced healing efficiency to approximately 46%.

Despite these advances, all capsule-based systems share a fundamental single-use limitation: once capsules along a given crack path are ruptured, no further healing is possible at that location. Vascular healing systems address this single-use constraint by delivering agents through refillable microchannel networks [86], [87], [88].

Toohey et al. (2007) introduced a biology-inspired self-healing system that overcame the single-use limitation of microcapsule approaches by employing a three-dimensional microvascular network embedded in a substrate beneath a brittle epoxy coating [60]. Modeled

after the dermal capillary system in human skin, the architecture used 200 μm diameter microchannels fabricated via direct-write assembly to continuously deliver DCPD healing agent to crack sites in the coating. There, the agent polymerized upon contact with Grubbs' catalyst particles dispersed within the coating. This design enabled repeated autonomous healing of the same crack location; the work demonstrated up to seven consecutive healing cycles with 10 wt% catalyst, achieving a peak healing efficiency of 70%. The number of successful healing cycles was strongly dependent on catalyst concentration, with specimens containing 2 wt% and 5 wt% catalyst achieving a maximum of only three (3) or four (4) cycles, respectively. SEM analysis revealed progressive build-up of polymerized DCPD film on the fracture surface with each healing cycle. This system was most limited by depletion of the active catalyst, rather than by depletion of the healing agent supply, and the authors proposed that future interdigitated dual-network designs delivering two-part chemistries could potentially achieve unlimited healing capabilities. Building on Toohey et al.'s work, Hamilton et al., achieved nearly full recovery over fifteen (15) consecutive cycles with pressurized active pumping [61].

Key research from Esser-Kahn et al. (2011), introducing the Vaporization of Sacrificial Components (VaSC) method, enabled the fabrication of microvascular networks within fiber-reinforced composites [89]. In this work, researchers wove sacrificial polylactic acid fibers into fiber preforms and subsequently removed these fibers via catalyzed depolymerization at approximately 200°C under vacuum using tin(II) oxalate catalyst. This produced hollow channels ranging from 20 to 500 μm in diameter with lengths exceeding one meter. The resulting networks demonstrated pluripotent functionality: the same composite could be reconfigured by changing the circulating fluid to achieve thermal management, electromagnetic modulation, electrical conductivity tuning, or chemical reactivity.

While vascular systems enable repeatable healing, the tediousness of the channel fabrication process and the risk of channel blockage have limited its practical adoption [90].

The thermoplastic interleaf concept places thin thermoplastic films or fabrics between composite plies during layup [91]. When the composite is heated above the melting temperature of the interleaf material, the molten thermoplastic flows into delamination cracks and reforms physical chain entanglements upon cooling, bonding the crack faces [92], [93], [94].

One of the most extensively studied interleaf materials is poly(ethylene-co-methacrylic acid) (EMAA) [95]. Meure et al. (2009) was the first work demonstrating that EMAA is a highly effective healing agent in an epoxy system, achieving up to 85% recovery of critical stress intensity factor and over 100% recovery of sustainable peak load at 150°C for 30 minutes without any externally applied pressure [96]. This study identified a pressure-driven delivery mechanism in which bubbles formed by condensation reactions between EMAA carboxylic acid groups and epoxy hydroxyl groups expand during heating, forcing larger volumes of molten healing agent into the fracture plane.

Varley et al. (2013) compared six (6) thermoplastic healing agents over four (4) healing cycles at 150°C and found that EMAA, poly(ethylene glycol) methacrylate (PEGMA), and ethylene-vinyl acetate (EVA) showed increasing load recovery with repeated healing [97]. They also found that polyvinyl butyral (PVB), styrene-ethylene-butylene-styrene (SEBS), and acrylonitrile butadiene styrene (ABS) showed sharp declines in load recovery. Rheological measurements correlated superior healing performance with liquid-like viscoelastic behavior at the healing temperature. Pingkarawat et al. (2013) further demonstrated that EMAA stitches in carbon fiber/epoxy composites fully restored both static fracture toughness and fatigue delamination resistance over five consecutive healing cycles [98].

While thermoplastic interleaf healing has shown significant repeatability and feasibility advantages over capsule and vascular network systems, it faces one serious limitation: the bonds formed during thermoplastic interleaf healing are physical in nature, relying on chain interdiffusion and entanglement rather than covalent bond reformation [65]. The reliance on physical entanglement represents a fundamental ceiling on the structural reliability of thermoplastic interleaf healing, and it is this ceiling that motivates the exploration of covalent exchange chemistries reviewed in the following section.

Covalent Adaptable Networks

Covalent adaptable networks (CANs) are polymer networks containing reversible covalent crosslinks that can undergo exchange reactions in response to an applied stimulus, typically heat [67], [72], [99], [100]. CANs are classified into two types based on their exchange mechanism. In dissociative CANs, such as Diels–Alder networks, a crosslink is first broken and then reformed, temporarily reducing network connectivity [101], [102]. Chen et al. (2002) provided the earliest demonstration of intrinsic healing using a Diels–Alder network, recovering approximately 50% of fracture load after a thermal cycle [103].

Diels-Alder systems are constrained by narrow processing windows and transient loss of network integrity during the retro-Diels-Alder step [104]. In associative CANs, a new bond forms simultaneously with cleavage of an existing bond, maintaining constant crosslink density throughout the exchange [105], [106]. The material never passes through a de-crosslinked state, preserving dimensional stability and insolubility at all temperatures [107].

Vitrimer Chemistry

Montarnal et al. (2011) demonstrated that epoxy networks catalyzed by zinc acetylacetonate could undergo transesterification exchange, enabling the permanently

crosslinked network to be reshaped, welded, and reprocessed without loss of crosslink density [68]. The viscosity decreased with temperature following an Arrhenius relationship analogous to inorganic glasses, prompting the term “vitrimer,” derived from the Latin word *vitrum*, meaning “glass.” Below a characteristic topology freezing transition temperature (T*v*), exchange reactions are kinetically frozen. Above T*v*, exchange enables macroscopic network rearrangement.

Since the original transesterification vitrimer, numerous exchange chemistries have been explored, including vinylogous urethane transamination, dioxaborolane metathesis, imine exchange, and disulfide exchange [108], [109], [110], [111]. The proliferation of exchange chemistries across the vitrimer literature has increasingly been directed toward two interrelated objectives: (1) enabling end-of-life recycling of fiber-reinforced thermoset composites [112]; and (2) developing materials capable of in-service damage repair [113].

Fiber-reinforced vitrimer composites are distinguished from conventional thermoset composites by their capacity for reprocessing, recycling, welding, and self-healing, with the dynamic covalent matrix enabling stress relaxation and network rearrangement while retaining mechanical performance comparable to traditional thermosets [113], [114]. Epoxy vitrimers based on transesterification have been the most extensively studied matrix systems for these applications. Chabert et al. (2016) provided the first demonstration that transesterification vitrimer composites containing over 50 volume percent continuous glass fiber could be repeatedly welded at their interfaces through hot-pressing above T*v* [115]. The dynamic exchange mechanism enabled the formation of covalent bonds across the weld line, producing joints whose mechanical integrity approached that of the pristine laminate. This work established the fundamental principle that vitrimer matrices can form structural joints between composite plies through interfacial bond exchange.

Biswal et al. (2023) extended the welding concept by demonstrating that ultrasonic energy could activate transesterification exchange in glass and carbon fiber vitrimer composites, producing welded joints in seconds rather than the hours required by hot-press methods [116]. The ultrasonic process provided sufficient thermal energy at the weld interface to initiate dynamic bond exchange and polymer chain interdiffusion, and the joints could be broken and re-welded up to five cycles with increasing strength at each iteration. This result demonstrated that vitrimer composite joining need not rely on oven-based thermal cycles, broadening the range of potential repair and assembly methods.

Martinez and Nutt (2024) further advanced vitrimer composite joining by adapting resistance welding to transesterification vitrimer carbon fiber composites [117]. Weld strengths matched or exceeded those of specimens consolidated by the manufacturer-recommended oven cure protocol, and repeated weld–break–reweld cycles over five iterations produced an average strength increase of 65% relative to the initial weld. The progressive strengthening with each re-weld cycle is a distinctive feature of vitrimer composites that has no analogue in conventional thermoset or thermoplastic systems, and it suggests that vitrimer interfaces may improve with repeated thermal activation.

While the transesterification systems described above require metal catalysts (typically zinc acetylacetonate) to achieve practically useful exchange rates, disulfide exchange vitrimers have attracted particular attention because aromatic disulfide bonds undergo radical-mediated exchange without any external catalyst [69], [70]. This eliminates the practical concerns of catalyst cost, leaching, and long-term deactivation that affect transesterification vitrimers in service [118], [119].

Ruiz de Luzuriaga et al. (2016) demonstrated the first fiber-reinforced vitrimer composite based entirely on disulfide exchange chemistry, using diglycidyl ether of bisphenol A (DGEBA) cured with 4-aminophenyl disulfide (4-APD) as the sole hardener [72]. Because every crosslink in the network contains a disulfide bond at its center, the entire matrix is capable of dynamic exchange above the topology freezing temperature. Fully cured DGEBA/4-APD prepreg sheets could be hot-pressed into consolidated laminates with indefinite shelf life because the dynamic bonds enable interfacial welding whenever heat and pressure are reapplied. Glass fiber composites fabricated from these prepregs achieved an interlaminar shear strength (ILSS) of 37 ± 3 MPa and flexural strength of 595 ± 39 MPa, values comparable to conventional epoxy composites. Critically, delamination damage introduced by ILSS testing was fully repaired at 200°C and 100 bar for 10 minutes, recovering ILSS values statistically identical to pristine specimens. This work established that disulfide-based vitrimer matrices can achieve both structural-grade mechanical properties and complete interlaminar damage recovery.

Si et al. (2020) advanced disulfide vitrimer composites by developing a catalyst-free epoxy system with high aromatic disulfide crosslink content, achieving a glass transition temperature of 147°C and tensile strength of 63.1 MPa in the neat resin [120]. Carbon fiber composites fabricated with this dual disulfide matrix exhibited a storage modulus of 10.5 GPa and tensile strength of 334 MPa. The resin matrix could be fully dissolved in dithiothreitol solution at 90°C within one hour, enabling complete recovery of the carbon fiber reinforcement. The recycled fibers were reformed into new composite laminates that retained a storage modulus of 8.2 GPa and tensile strength of 320.9 MPa, demonstrating that disulfide vitrimer composites enable closed-loop fiber recycling with minimal property degradation.

The structural viability of disulfide vitrimer composites for aerospace applications was evaluated by Markaide et al. (2022), who performed a comprehensive mechanical characterization of a carbon fiber composite using a new aeronautic-grade epoxy vitrimer with aromatic disulfide crosslinks [121]. The testing campaign encompassed tension, compression, ILSS, in-plane shear, open-hole tension and compression, filled-hole compression, and Mode I and Mode II interlaminar fracture toughness across room temperature, hot-wet, and elevated-temperature conditions. The disulfide vitrimer composite exhibited mechanical properties competitive with conventional aerospace epoxy systems under most test conditions, although elevated temperature performance remained a concern. This work represented the most comprehensive mechanical evaluation of a disulfide vitrimer composite to date and demonstrated that the dynamic chemistry does not inherently compromise structural performance at the laminate level.

Perrin et al. (2022) addressed the fatigue behavior of vitrimer composites directly, demonstrating that fatigue damage in carbon fiber vitrimer laminates based on transesterification chemistry could be reversed by heating above T*v* [122]. Using molecular dynamics simulations alongside experimental fatigue testing, the authors showed that intermittent healing cycles could postpone fatigue failure indefinitely, because each thermal cycle re-established covalent connectivity across fatigue-generated microcracks in the vitrimer matrix. This is the most directly relevant precedent for the present work, as it demonstrates the principle that vitrimer chemistry can reverse cyclic damage accumulation in fiber-reinforced composites. However, the system studied by Perrin et al. employed a full vitrimer matrix throughout the composite, rather than targeting the dynamic bonds selectively at the interlaminar interfaces.

In subsequent work, Perrin et al. (2024) investigated cyclic delamination-healing in woven carbon fiber composites with a bio-based benzoxazine vitrimer matrix [123]. Short-beam shear specimens were subjected to four consecutive delamination-healing cycles at 170°C and 1 MPa. Specimens healed for 60 minutes exhibited substantial ILSS recovery across all four cycles, although a gradual decrease in recovered strength was observed with each successive cycle. This study provided the first systematic evaluation of repeated delamination-healing performance in vitrimer composites and highlighted two important findings: first, that healing duration significantly affects recovery quality, and second, that cumulative property degradation occurs across multiple healing cycles even in a full vitrimer matrix system.

A critical observation across the vitrimer composites literature is that every published system places the dynamic covalent bonds throughout the entire polymer matrix. The fiber reinforcement is fully embedded in a vitrimer resin that serves simultaneously as the structural matrix and the healing medium. While this approach has demonstrated impressive healing and recycling capabilities, it imposes several practical constraints. The vitrimer resin must satisfy all requirements of a structural composite matrix, processability, fiber wetting, thermal stability, and environmental resistance, while also providing rapid exchange kinetics for healing. These requirements often conflict. Catalysts that accelerate exchange also promote creep under sustained loading at elevated temperatures, and disulfide bonds that enable healing also introduce potential sites for environmental degradation [124]. Furthermore, the full vitrimer matrix approach requires complete reformulation of the composite material system, precluding its application to existing material qualifications and manufacturing workflows.

No published work has investigated the alternative strategy of placing dynamic covalent bonds exclusively at the interlaminar interfaces while retaining a conventional matrix for

structural load bearing. Such an approach would remove the healing function from the structural matrix function, potentially enabling interlaminar healing in composite systems that are not amenable to full vitrimer reformulation. It is this unexplored strategy that the present work investigates, using neat 4-APD as a standalone interply healing agent rather than as a component of a vitrimer resin formulation.

Disulfide Exchange Chemistry and 4-APD

Understanding the molecular-level mechanism of disulfide exchange is essential for this thesis because the healing capability of the interply vitrimer coating depends entirely on whether, and how rapidly, broken sulfur–sulfur bonds can reform across a damaged interface when heat and pressure are applied [125], [126]. The disulfide bond (S–S) has a bond dissociation energy of approximately 60 kcal/mol (251 kJ/mol) for typical dialkyl disulfides, making it roughly 25 - 35% weaker than a carbon–carbon bond and the weakest covalent link in most molecular chains [127]. For aromatic disulfides the bond dissociation energy drops further to approximately 48 kcal/mol because the aromatic ring distributes the unpaired electron of the broken bond across multiple atoms in the ring. This stabilizes the resulting radical and lowers the energy required to form it [128]. This stabilization is the fundamental reason aromatic disulfides undergo dynamic exchange at substantially lower temperatures than aliphatic disulfides, and it is why an aromatic disulfide was selected for the vitrimer formulation in this work [73].

The exchange mechanism proceeds through a [2+1] radical chain transfer process, as established theoretically by Matxain et al. (2016) and validated experimentally by Nevejans et al. (2016) [128], [129]. When an S–S bond undergoes homolytic cleavage, breaking such that each sulfur retains one electron from the shared pair, two sulfur-centered radicals called thiyl radicals are produced. A free thiyl radical then attacks an intact S–S bond on a neighboring molecule,

temporarily bonding to both sulfur atoms to form a transient three-sulfur chain. This intermediate immediately fragments, releasing a new thiyl radical and leaving behind a newly formed disulfide bond that incorporates the attacking sulfur. The process is a chain reaction: each exchange event consumes one radical but generates a new one, so the reaction propagates without requiring new radicals at every step. Nevejans et al. confirmed this mechanism by showing that a substoichiometric amount of the radical scavenger TEMPO completely shut down exchange: a result only possible if the reaction propagates through a chain, where terminating even a few radicals halts the entire sequence. They also demonstrated a parallel pathway: when nucleophilic catalysts such as triethylamine are present, thiolate anions (RS^-, sulfur atoms carrying a negative charge rather than an unpaired electron) are generated, and these undergo their own exchange by attacking one sulfur of an intact S–S bond and displacing the other as a new thiolate. In the present system, radical-mediated exchange serves as the primary healing mechanism. Although unreacted amine groups in the resin environment could theoretically accelerate exchange through the thiolate pathway, this contribution has not been isolated experimentally in this work and is not relied upon in the proposed healing mechanism.

4-Aminophenyl disulfide (4-APD), formally named bis(4-aminophenyl) disulfide, is a symmetrical molecule consisting of two para-aminophenyl rings connected by a central S–S bridge [130]. The molecule is bifunctional by deliberate design: the primary amine groups ($–NH_2$) at each end serve as reactive handles for covalent bond formation, while the central disulfide bridge provides the thermally activated exchange capability described above [131]. The position of the amine on the rings matters. Azcune and Odriozola (2016) established that the para-substituted 4-APD produces vitrimers with higher topology freezing temperatures and better mechanical properties than the ortho-substituted isomer (2-APD), because the para position

allows more effective radical stabilization during exchange [73]. When 4-APD is used as an epoxy hardener, its amine groups react with the oxirane (epoxide) groups of the resin through ring-opening addition [132]. An epoxide is a strained three-membered ring of two carbons and one oxygen; the nitrogen's lone electron pair attacks a ring carbon, breaking the strained carbon–oxygen bond and forming a new carbon–nitrogen bond plus a hydroxyl group. Each primary amine carries two active N–H bonds and can therefore open two epoxide rings in sequence, and because 4-APD has two amine groups, a single molecule can form up to four crosslinks and every one of which contains a disulfide bond at its center [133].

The same amine chemistry that builds the vitrimer network also anchors 4-APD to plasma-activated ply surfaces [134]. Atmospheric plasma treatment generates oxygen-containing functional groups on carbon fiber and UHMWPE surfaces, including carboxyl (–COOH) and epoxide groups [135], [136]. The primary amines of 4-APD react with surface carboxyl groups to form amide bonds (–CO–NH–) through a condensation reaction, and with surface epoxide groups through the same ring-opening aminolysis that occurs during epoxy cure [137], [138]. Both pathways produce strong covalent bonds that tether 4-APD to the ply surface and position the disulfide bridge at the interply interface [139]. During a healing cycle, when heat and pressure bring damaged crack faces back into contact, the S–S bonds spanning the interface undergo radical chain transfer exchange to reform covalent linkages across the separated surfaces, thereby restoring molecular continuity without any catalyst [129].

Because the radical chain transfer mechanism is catalyst-free, the system avoids the practical concerns of catalyst leaching, deactivation, or chemical incompatibility with the UHMWPE matrix over the service life of the composite [140], [141]. The energy barrier for the

chain transfer step is only approximately 10 kcal/mol once radicals are generated, and the healing temperature of 120°C provides sufficient thermal energy to drive homolytic cleavage of the aromatic S–S bonds while remaining safely below the UHMWPE melting temperature of 130–136°C [142].

Carbon Fiber and UHMWPE

Ultra-high molecular weight polyethylene (UHMWPE) is a linear polyethylene with molecular weights typically exceeding 3.5 million g/mol, conferring exceptional abrasion resistance, impact toughness, and chemical inertness [76], [143]. These properties have established UHMWPE as a material of choice in biomedical implants, ballistic protection, and marine applications [33]. However, UHMWPE presents significant processing challenges for composite fabrication. It's extremely high melt viscosity --- a direct consequence of the exceptionally long polymer chains and their extensive entanglement network --- severely limits matrix flow during consolidation, making conventional impregnation of continuous fiber reinforcements impractical [32].

Nonwoven fiber architectures offer a solution to the impregnation challenge. In a nonwoven mat, discontinuous fibers are randomly distributed within a plane rather than arranged in ordered tows or weaves [31]. This random architecture creates an open, porous structure with short inter-fiber distances that can be penetrated by the UHMWPE melt during hot-press consolidation, provided that sufficient temperature and pressure are applied to overcome the high viscosity [32]. The combination of carbon fiber reinforcement with a UHMWPE matrix in a nonwoven architecture produces a composite system that leverages the high specific stiffness and strength of carbon fiber with the damage tolerance, chemical resistance, and low friction coefficient of UHMWPE.

Despite these advantages, the CF/UHMWPE system presents two characteristics that are directly relevant to the present work. First, the inherently low surface energy of UHMWPE limits interfacial adhesion with carbon fiber, resulting in interlaminar properties that are generally lower than those achieved in epoxy-based carbon fiber composites [144]. This weak interlaminar adhesion makes the CF/UHMWPE system particularly susceptible to delamination, reinforcing the motivation for interply healing strategies. Second, as mentioned before, both carbon fiber and UHMWPE present chemically inert surfaces that resist bonding with external agents [74], [75], [76]. Carbon fiber surfaces, particularly after desizing, consist primarily of graphitic basal planes with limited reactive functionality [74]. UHMWPE surfaces consist of nonpolar methylene chains with no inherent reactive sites for covalent bonding [76]. This dual inertness means that any interply healing agent applied to this composite system cannot rely on spontaneous chemical interaction with the ply surfaces; an activation strategy such as plasma treatment is required to generate the reactive functional groups necessary for covalent attachment.

No published work has addressed interlaminar healing in a UHMWPE-based composite system of any kind. The combination of UHMWPE's processing constraints, inert surface chemistry, and low melting temperature creates a unique set of challenges that distinguish this material system from the epoxy-based composites in which all prior healing work has been conducted.

Plasma Surface Treatment of Carbon Fiber and UHMWPE

Plasma treatment is a method of modifying polymer and fiber surfaces to improve adhesion and wettability [145], [146]. This method is used to tailor the surface properties of a material without changing the bulk material characteristics [147]. Plasma is described as gas that

contains free electrons and ions, and it is referred to as the fourth state of matter [145]. When plasma is directed at a surface, radiation and energetic species work together to break covalent bonds in the outermost molecular layers, creating radical sites that react with atmospheric oxygen to form polar functional groups including hydroxyl, carbonyl, carboxyl, and epoxide [78], [148]. At the same time, ion bombardment creates nanoscale roughness that increases the material's surface adhesion. These characteristics can be controlled and tuned through parameters like gas composition, power, pressure, and exposure time [149], [150]. Overexposure of plasma treatment can cause degradation and aging, so the conditions must be optimized accordingly.

Blackman et al. (1994) investigated plasma treatment for carbon/thermoplastic adhesion and saw a significant increase in the material's surface adhesion after plasma treatment [151]. Their findings demonstrated that abrasion and solvent cleaning of the surface alone was insufficient to achieve effective joining at the composite/adhesive interface at low applied load. But, when oxygen plasma treatments were applied, the fracture energy increased and shifted the failure away from the interface. The researchers primarily attributed this to the plasma treatment's increase in polar oxygen functionality rather than surface roughness.

Mandal et al. (2025) show that carbon fiber surface functionality directly affects wettability and interfacial shear strength (IFSS) [152]. The researchers removed 60% of the surface functional groups from sized carbon fiber and found that IFSS decreased 12%. Their analysis indicated that chemical bonding could account for 20% of vitrimer composite load-bearing capabilities. However, for vitrimers to achieve good adhesion with inert surfaces, covalent bonds must be integrated at the interface. Plasma treatment allows anchoring groups like hydroxyl to form on the source, thereby creating an opportunity for covalent bond exchange

with vitrimer additives. This critical three-part reaction between the polymer surface, plasma treatment, and vitrimers forms robust interfacial linkages that improve welding and bonding performance [153].

Dominguez-Lopez et al. (2021) investigated the effect of atmospheric plasma treatment on UHMWPE wettability over a ninety-day (90-day) observation period [154]. The treatment reduced the water contact angle from an initial 85° to nearly 40° immediately after exposure, with the effect being dependent on both exposure time and distance from the plasma source. Raman spectroscopy revealed that the improved wettability coincided with an increase in the orthorhombic crystalline phase and a reduction in the amorphous phase. However, significant hydrophobic recovery occurred over the first 30 days, after which the contact angle stabilized at 66° and 73° for samples placed two (2) cm and four (4) cm from the plasma, respectively, still evidencing significant improvement compared to untreated material.

Summary and Research Gap

The literature reviewed in this chapter establishes that disulfide exchange chemistry enables catalyst-free healing through a radical chain mechanism at moderate temperatures [129], [155], that plasma treatment introduces reactive functional groups onto inert carbon fiber and UHMWPE surfaces [156], [157], and that interlaminar property recovery is achievable through externally activated thermal protocols compatible with existing maintenance workflows [64], [65]. Most of the published vitrimer composite systems place the dynamic disulfide bonds throughout the entire polymer matrix rather than selectively at the interlaminar interfaces [67]. At the time of writing, no published work has applied 4-APD directly to composite ply surfaces as a standalone molecular bridge, combined plasma activation with disulfide exchange chemistry at composite interfaces or addressed healing of any kind in a CF/UHMWPE-based composite

system. These three gaps converge on an opportunity that the present work is designed to address.

This thesis investigates the feasibility of combining atmospheric plasma surface activation with neat 4-APD applied at interply interfaces to create a healable carbon fiber/UHMWPE nonwoven composite. The system is described as healable rather than self-healing. Damaged components must be identified, removed from service, and placed in a heated press at 120°C. Four composite variants isolate the individual and combined contributions of each treatment. A baseline with no treatment, a plasma-only variant, a 4-APD-only variant, and a combined plasma-plus-4-APD variant. The last variant tests the central hypothesis that plasma-generated functional groups provide superior covalent anchor sites for 4-APD, resulting in stronger initial bonding and more effective property recovery after fatigue-induced delamination. Specimens undergo three-point bend fatigue followed by a healing cycle and are re-tested. Additional characterization by Fourier transform inferred, water contact angle, X-ray CT, and DMA provide insight into the damage and healing response.

CHAPTER THREE – MATERIALS AND METHODS

This chapter describes the materials, fabrication procedures, and experimental methods employed in this work. Four variants of composite panels were prepared using nonwoven carbon fiber (CF)/UHMWPE mats, atmospheric plasma surface treatment, 4-aminophenyl disulfide interply treatment, and compression molding. Each variant was fabricated with a distinct combination of plasma treatment and 4-APD application designed to isolate the individual contributions of each treatment to interlaminar bonding and healing performance. The variant designations and treatment combinations are presented in **Table 3.1** The following subsections detail each step of the experimental program in the order it was executed: material fabrication, surface treatment, 4-APD application, composite fabrication, mechanical testing, the healing protocol, characterization techniques, and data analysis.

Nonwoven Mat Fabrication

CF/UHMWPE nonwoven mats were fabricated using an in-house wet-laid system. Approximately 14 grams of 1-inch-long carbon fibers and 14 grams of 1-inch-long UHMWPE fibers were suspended in an aqueous slurry.

The system was allowed to agitate for 15 minutes to achieve a homogeneous fiber distribution before the water was drained through a forming screen. Residual water was removed by vacuum extraction, and the mats were dried of remaining moisture. This process produced a nonwoven mat with a 50/50 weight percent ratio of carbon fiber to UHMWPE fiber and a target areal weight of 300 GSM. Each mat was fabricated at a nominal dimension of 12 × 12 inches. The wetlaid setup used in this work is shown in **Figure 3.1.**

Table 3.1. Variant naming conventions and treatment combinations.

Variant Name	Plasma Treatment	4-APD Application	Purpose
CN	No	No	Baseline reference/control
CP	Yes	No	Isolate plasma treatment effect
CD	No	Yes	Evaluate 4-APD on untreated surfaces
CPD	Yes	Yes	Test central hypothesis

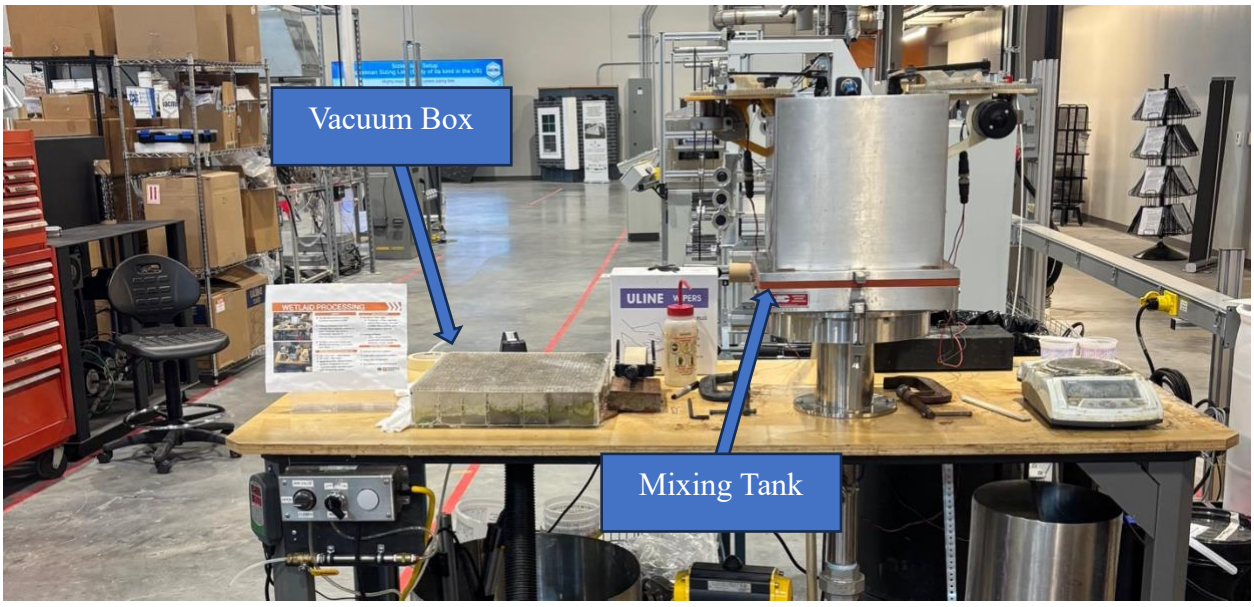


Figure 3.1. Photograph of wetlaid system showing the mixing tank and vacuum box.

The dried nonwoven mats were placed in an 11 × 11-inch flat mold and consolidated at 330°F for 15 minutes under a force of 22,000 lbs. This initial hot-pressing step served to partially melt the UHMWPE fibers into a continuous matrix phase while maintaining the spatial distribution of the carbon fiber reinforcement. It also served to create a uniform surface that could then be activated with plasma or coated with 4-APD. The consolidated mats were then cut into approximately 5.5 × 5.5-inch squares. A total of forty squares were produced so that each of the four composite variants could be assembled from a unique set of 10 plies. For clarity throughout the remainder of this document, these consolidated and cut squares are referred to as plies.

Composite Fabrication

Each composite panel was assembled from a unique set of 10 plies stacked to form a laminate. The four variants were fabricated according to the following protocols.

Variant CN received no surface treatment and no 4-APD application. The 10 plies were stacked and consolidated directly. This variant serves as the baseline against which all other variants are compared. Variant CP had each ply plasma treated on both sides according to the parameters listed in the plasma treatment section below**.** The treated plies were kept in sealed bags and consolidated within 1 hour of treatment to minimize the effects of hydrophobic recovery. No 4-APD was applied. Variant CP isolates the effect of plasma surface activation on interlaminar bonding in the absence of 4-APD. Variant CD had 4-APD solution applied to both sides of each ply without any preceding plasma treatment. This variant evaluates the ability of 4-APD to bond to and heal untreated ply surfaces, establishing a comparison point for assessing the added value of plasma activation. Variant CPD had each ply plasma treated on both sides before

4-APD solution was applied to both treated surfaces. This variant evaluates the central hypothesis of this thesis: Plasma-generated functional groups provide superior covalent anchor sites for the amine groups of 4-APD, resulting in stronger initial interlaminar bonding and more effective healing after fatigue-induced delamination damage.

For all variants, the 10 plies were stacked on an 11 × 11-inch steel plate preheated to 160°C. A second preheated plate was placed on top of the stack and the assembly was transferred to the heated press. The panels were consolidated at 160°C under a force of 5,000 lbs for 3 minutes and then allowed to cool to room temperature under sustained pressure. The consolidation temperature of 160°C was selected to exceed the melting temperature of the UHMWPE matrix (~130 – 136°C), ensuring full matrix flow and interply bonding, while remaining well below the thermal degradation temperature of 4-APD. After cooling, the consolidated panels were removed from the press and cut into test specimens on a waterjet cutting system according to the specimen dimensions prescribed by the relevant ASTM standards for each test method. A picture of the stacked plies on the plate and the resultant consolidated panel is shown in **Figure 3.2.**

4-Aminophenyl Disulfide

The interply healing compound used in this work was 4-aminophenyl disulfide (4-APD; CAS 722-27-0; MW 248.37 g/mol; Tm ≈ 77–78°C), sourced from Sigma-Aldrich. In the published fiber-reinforced composites literature, 4-APD has been used almost exclusively as a curing agent for epoxy resins [158]. However, in the present work, 4-APD is not mixed with any resin system. Instead, it is applied neat as a standalone bifunctional compound whose amine



Figure 3.2. Ten plies stacked on plate (left) and resultant consolidated panel (right).

groups bond to plasma-activated ply surfaces and whose central disulfide bridge provides the thermally activated exchange mechanism for interply healing. 100 mg 4-APD was dissolved in 10 ml of ethanol by stirring. 6 ml of the solution containing 60 mg of 4-APD was sprayed on each side of the composite plies for Variants CD and CPD. The setup and application of 4-APD is shown in **Figure 3.3.** For Variant CD, each ply had 4-APD solution sprayed onto both sides without any preceding plasma treatment. For Variant CPD, 4-APD was applied immediately after plasma treatment to maximize the availability of reactive oxygen-containing functional groups on the ply surface before hydrophobic recovery could reduce the surface energy. After spraying, the solvent was allowed to evaporate at room temperature before the plies were stacked for consolidation.

Plasma Surface Treatment

Atmospheric plasma surface modification was performed on the plies designated for Variants CP and CPD using a Plasmatreat rotary jet (model RD1004) powered by a Plasmatreat



Figure 3.3. 4-APD solution (left) and 4-APD application to composite plies of Variants CD and CPD (right).

FG5001 Openair-Plasma Generator, supplied by Plasmatreat GmbH (Steinhagen, Germany). The plies were secured to an x-y stepper motor-controlled translation stage. The plasma jet was held stationary while the stage traversed beneath it at a controlled speed. Each ply was treated on both sides at a speed of 2.08 inches per second. After treatment, the plies were immediately sealed in airtight bags before 4-APD application or composite consolidation. The complete set of plasma treatment parameters is provided in **Table 3.2**. The plasma treatment setup is shown in **Figure 3.4.**

The plasma treatment parameters were determined empirically through a series of preliminary trials. Early trials with nozzle-to-surface distances less than 4 cm and speeds slower than 2.08 in/s resulted in visible thermal damage to the UHMWPE component of the nonwoven mat, including localized melting and, in extreme cases, charring. The UHMWPE fibers are particularly susceptible to thermal degradation because of their relatively low melting temperature of approximately 130 to 136°C. The parameters reported in **Table 3.2** represent the most aggressive treatment achievable without introducing visible thermal damage to the ply surface.

Fourier Transform Infrared (FTIR)

Fourier transform infrared (FTIR) spectroscopy was used to assess whether the atmospheric plasma treatment produced detectable chemical changes at the surface of the consolidated layers. Neat UHMWPE fibers were consolidated into films at 160 °C under 11 tons of pressure and subsequently subjected to atmospheric plasma treatment at five different traverse speeds. Neat UHMWPE was chosen so that the FTIR equipment in this work could interact with

Table 3.2. Complete list of plasma treatment parameters.

Parameter	Value
Gas	Atmospheric
Nozzle Diameter	1 in
Nozzle to Mounting Plate Distance	4 cm
Air Pressure	400 kPa
Plasma Pressure	300 kPa
Plasma Application	2.08 in/s
Plasma Frequency	21 kHz
Output Voltage	300 V
Plasma Cycle Time (PCT)	100 %

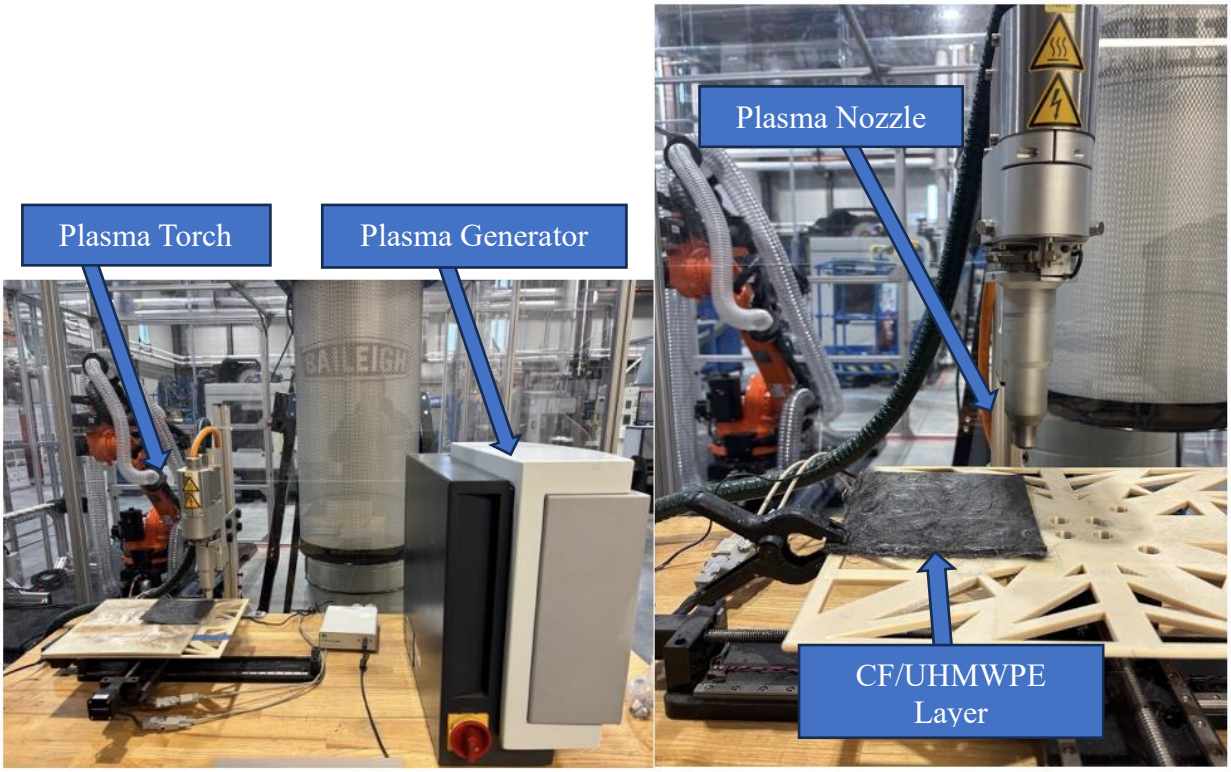


Figure 3.4. Plasma treatment setup.

the surface. Prior tests with dry fiber were inconclusive and difficult to test. Sample 1 was treated at 1 in/s, Sample 2 at 1.25 in/s, Sample 3 at 2.08 in/s, Sample 4 at 2.60 in/s, and Sample 5 at 3.03 in/s. Higher traverse speeds correspond to shorter plasma dwell times over any given point on the surface, and therefore lower cumulative plasma exposure. Sample 3 was designed to mimic the plasma exposure used for the composite manufacturing.

Spectra were collected in attenuated total reflectance (ATR) mode, which requires no sample preparation beyond placing the treated surface in direct contact with the ATR crystal. All samples were analyzed within one hour of plasma treatment to minimize hydrophobic recovery. Between treatment and testing, samples were kept in sealed polyethylene bags to limit contamination and exposure to ambient moisture.

For each plasma-treated sample, multiple spectra were collected at different spot locations on the treated side to account for potential spatial non-uniformity in the plasma treatment. Each spectrum was exported as a CSV file containing wavenumber (cm^{-1}) and absorbance values. Spectra were imported into MATLAB for plotting and comparison, with each sample group color-coded according to its treatment speed. The entire mid-infrared region (approximately 500–4000 cm^{-1}) was examined. Attention was given to the 1350–1550 cm^{-1} region (CH_2 bending) and the 1600–1800 cm^{-1} region (C=O and C=C stretches), both of which are commonly reported as indicators of plasma-induced surface oxidation in polyethylene [159], [160], [161].

Water Contact Angle

Static water contact angle (WCA) measurements were performed to evaluate the effect of plasma treatment on the surface wettability of the composite plies. Measurements were conducted using a Kruss DSA 30 Contact Angle Goniometer. Deionized water droplets of 0.2 μL volume were dispensed onto the specimen surface at a rate of 1 μL/s using an automated syringe system. The contact angle was measured immediately after droplet deposition.

Specimens were prepared using the same methodology used to for FTIR. Strips of UHMWPE were cut out of the films of each sample and placed under the syringe to test the treated and untreated faces of the UHMWPE. A minimum of 3 measurements were taken at different locations across each specimen surface to account for local variability, and 2 specimens per variant were tested. All measurements were performed at ambient conditions of 20°C.

Three-Point Bend Fatigue Testing

Flexural fatigue testing was performed on an Instron 5965 universal testing machine equipped with a 5kN load cell. The specimens were loaded in three-point bending at a span length calculated according to ASTM 790 and as expressed in **Equation 3.1**

$$L = 16 \times T \tag{3.1}$$

In **Equation 3.1**, L is the span length in mm and T is the sample thickness in mm. The test was conducted at a frequency of 0.125 Hz, and a displacement-controlled amplitude of 2 mm. 10 mm diameter load nose and supports were used. Each specimen was subjected to 30

minutes of continuous cyclic loading, corresponding to 223 cycles at the selected frequency. A picture of the fatigue setup is shown in **Figure 3.5.**

The 30-minute fatigue duration was selected to induce measurable interlaminar damage without causing catastrophic specimen failure. This controlled level of damage is essential for evaluating healing effectiveness. The post-healing fatigue response can only be compared meaningfully to the virgin response if the specimen retains sufficient structural integrity to be re-tested. After the first fatigue test, all specimens underwent the healing cycle described in the following section. Following the healing cycle, specimens were returned to the Instron machine and subjected to a second fatigue test under identical loading conditions. The comparison of the virgin and healed fatigue degradation curves is the primary metric for evaluating the effectiveness of the 4-APD interply healing system. The peak load degradation behavior over the 223-cycle fatigue test was characterized by fitting each specimen's thickness-normalized peak load versus cycle number data to a logarithmic decay model of the form shown in **Equation 3.2.**

$$P(N) = a + b \cdot \ln(N) \tag{3.2}$$

Where P is the peak load per unit thickness (N/mm), N is the cycle number, a is the intercept, and b is the decay rate. The model parameters were determined by ordinary least squares regression on the log-transformed cycle number. The coefficient of determination (R^2) was computed for each fit to evaluate goodness of fit. This model was applied independently to each specimen in both the virgin and healed conditions, and the mean decay rates (b) were compared across variants to characterize differences in the rate of fatigue damage accumulation.

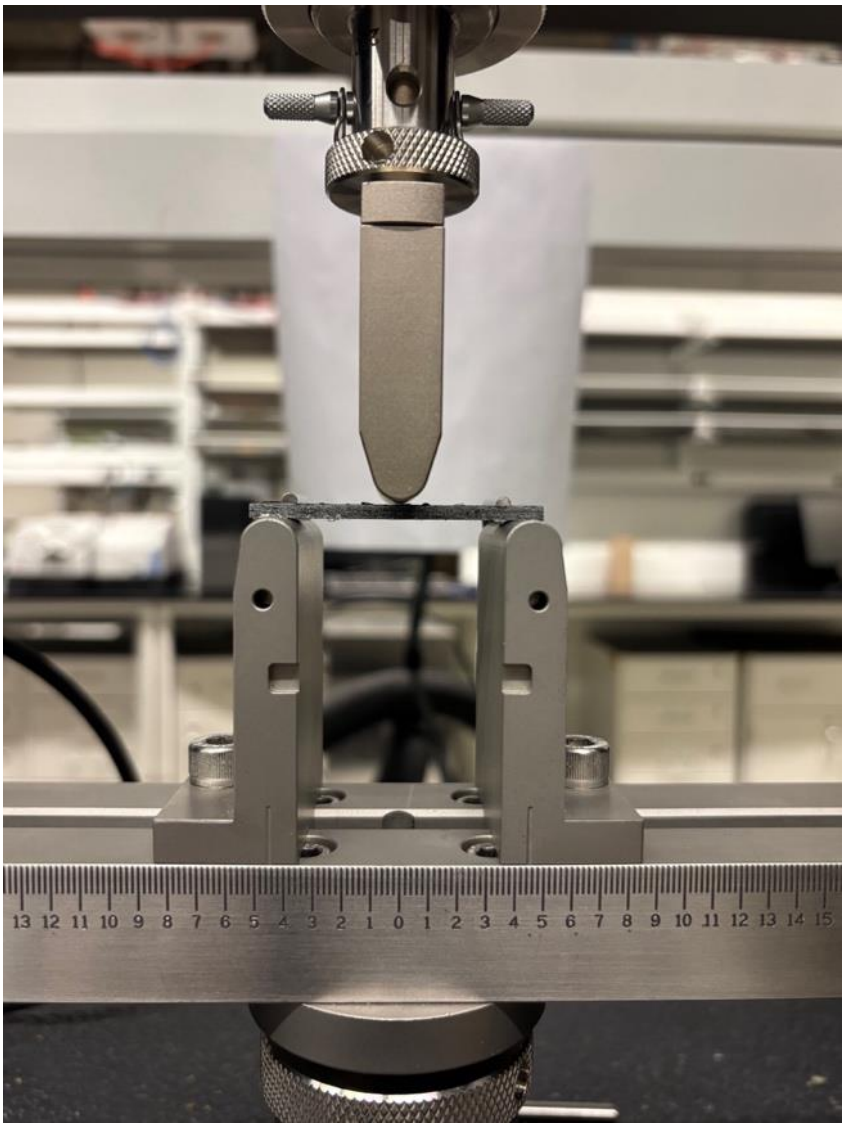


Figure 3.5. Three-point bend fatigue test setup.

Healing Protocol

The healing protocol was designed to activate the disulfide exchange chemistry of the 4-APD molecules at the interply interfaces while preserving the structural integrity of the UHMWPE matrix. Two competing thermal constraints define the processing window for healing. The lower bound is the temperature at which S-S metathesis becomes kinetically active in 4-APD, which must be exceeded for bond exchange across the delaminated interface to proceed. The upper bound is the melting temperature of the UHMWPE matrix, approximately 130 to 136°C, which must not be exceeded to avoid uncontrolled matrix flow and loss of laminate architecture.

A healing temperature of 120°C was selected to satisfy both constraints. Six specimens were healed simultaneously in each pressing cycle. The specimens were arranged on a Teflon release sheet to prevent adhesion to the press platens and placed into the heated press. A consolidation force of 0.75 tons (US) was applied for 1 hour at 120°C. The applied pressure serves a critical mechanical function: It brings the opposing faces of delamination cracks into intimate contact, which is a prerequisite for 4-APD molecules on opposing surfaces to undergo S-S metathesis exchange across the crack plane. Without sufficient crack-face contact, the disulfide exchange reaction cannot bridge the damaged interface regardless of temperature. After the 1-hour hold, the specimens were cooled to room temperature under sustained pressure before removal from the press.

Healing efficiency was quantified using **Equation 3.3.**

$$\text{Total Curve healing} = \frac{\int \left(\frac{P_{Healed}}{Healed_{Thickness}}\right)(c)dc}{\int \left(\frac{P_{Virgin}}{Virgin_{Thickness}}\right)(c)dc} \; x\; 100 \qquad (3.3)$$

In **Equation 3.3**, the integrals represent the areas under the normalized peak load versus cycle number curves for the healed and virgin conditions, respectively.

X-Ray Computed Tomography

The internal structure and damage state of the composites were investigated non-destructively using X-ray micro-computed tomography. Scans were performed using a Zeiss Xradia Context microCT system at a tube voltage of 40 kV with an exposure of 0.5 seconds, a pixel binning set to 2, and 3,201 projections. One specimen from Variant CN and one from Variant CPD were scanned at three distinct stages of the experimental program: (1) the undamaged (as-fabricated) condition; (2) the damaged condition (after the first 30-minute fatigue test); and (3) the healed condition (after the healing cycle). Scanning the same specimen at all three stages enables direct visualization of damage initiation, propagation, and recovery within a single sample. The X-ray micro-computed tomography setup is shown in **Figure 3.6.**

The reconstructed image stacks were analyzed using Dragonfly 3D software (Object Research Systems, Montreal, Canada) to quantify the internal porosity at each stage. The 4-APD coating is too small to distinguish in x-ray imaging but the effects of if its presence can be seen and quantified when comparing the damaged and healed states. The segmentation procedure consisted of the following steps. First, a grayscale thresholding operation was applied to identify all voxels corresponding to airspace, including both internal voids and the surrounding atmosphere. This region of interest (ROI) was designated “All Airspace.” Second, a separate

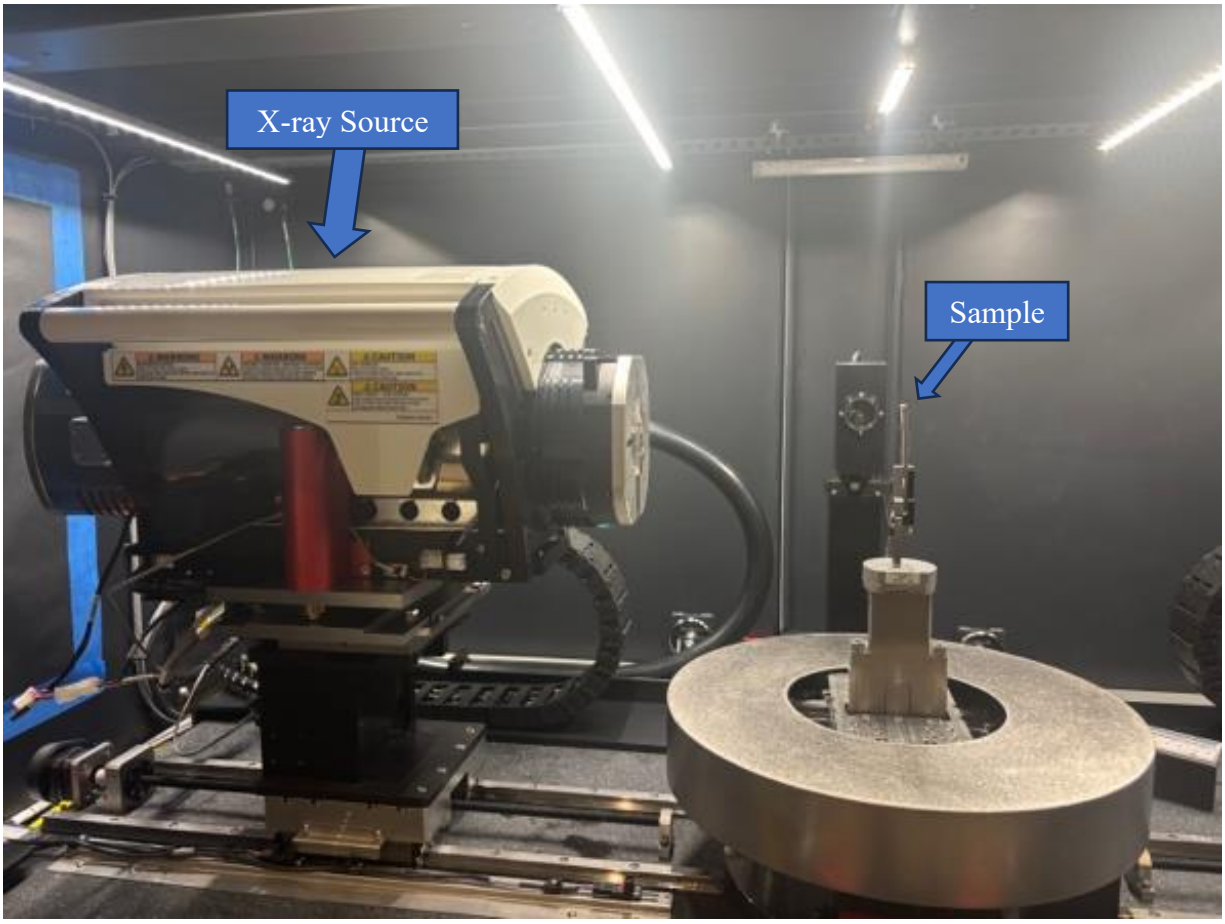


Figure 3.6. X-ray computed tomography setup.

threshold was applied to identify all solid-phase voxels, which included the carbon fiber and the UHMWPE matrix. A morphological closing operation was then applied to this solid-phase ROI. The closing operation identifies voxels that are completely enclosed by the segmented solid and incorporates them into the ROI, effectively filling internal gaps to produce a continuous volume representing the entire specimen envelope. This ROI was designated "Everything in Sample." Third, a Boolean intersection was computed between the "Everything in Sample" and "All Airspace" ROIs to isolate only the airspace voxels that fell within the specimen boundary. This final ROI was designated "Void" and represented the total internal porosity of the specimen at that stage. This visualized workflow is shown in **Figure 3.7.**

This segmentation procedure was repeated for each of the three stages for both the CN and CPD specimens. The volumetric porosity was calculated using **Equation 3.4.**

$$Porosity\ (\%) = \frac{V_{Void}}{V_{Sample}} \times 100 \tag{3.4}$$

In **Equation 3.4**, V_{Void} is the total volume of the "Void" ROI and V_{Sample} is the total volume of the "Everything in Sample" ROI. Both volumes were computed using the built-in volumetric measurement tools in Dragonfly 3D.

Dynamic Mechanical Analysis

Dynamic mechanical analysis (DMA) was performed on a TA DMA-850 in dual cantilever deformation at an oscillation frequency of 1 Hz and a strain amplitude of 3%. The temperature was increased from 25°C to 123°C at a rate of 3°C/min. Specimens with dimensions of 12.7 x 64 mm were cut from each composite variant. The storage modulus (E') was recorded as a continuous function of temperature.

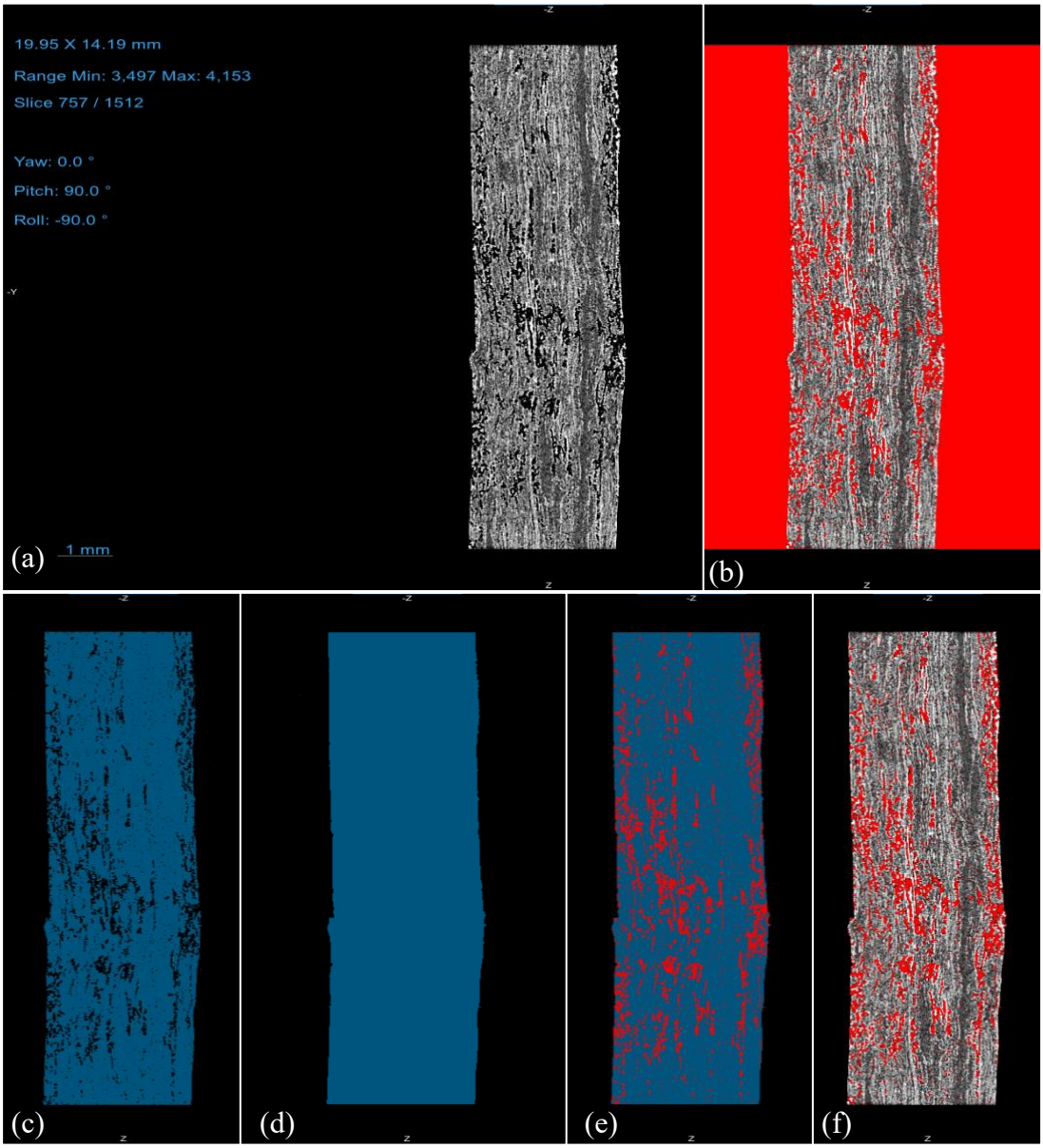


Figure 3.7. Visual depiction of Dragonfly workflow. (a) The imported image stack of the CN damaged state shown in the Y-Z plane at slice 757. (b) The ROI for "All Airspace" is created by thresholding. (c) The "All Airspace" ROI is inverted to capture everything that is not void. (d) The "close" command is executed to create the ROI for "Everything in Sample". (e) The two ROIs are intersected to find all the void within the sample. (f) The resultant "Void" ROI is overlayed on the original image stack.

Data Analysis and MATLAB Processing

Raw load-displacement time-series data from the Instron acquisition system were processed using a custom MATLAB script (R2021b, MathWorks) that identified individual loading cycles by detecting successive load maxima and extracted the peak load, valley load, loading stiffness, and crosshead displacement at peak load for each cycle. Peak load values were normalized by specimen thickness measured prior to each test condition to account for the reduction in cross-section produced by the healing consolidation cycle. Healing efficiency was computed as the ratio of the area under the thickness-normalized healed fatigue curve to the area under the corresponding virgin curve, evaluated by trapezoidal integration using **Equation 3.3.** All data are reported as arithmetic mean ± one standard deviation across all replicates within each variant.

CHAPTER 4 – RESULTS AND DISCUSSION

Fourier Transfer Infrared Spectroscopy

The FTIR spectra of all plasma-treated UHMWPE samples exhibit the characteristic features of polyethylene. The dominant absorption bands are centered near 2915 and 2847 cm^{-1}, corresponding to the asymmetric and symmetric C–H stretching vibrations of the CH_2 groups that make up the polyethylene backbone [162], [163]. A secondary cluster of peaks appears in the 1460–1470 cm^{-1} region, assigned to CH_2 bending (scissoring) vibrations, with additional bands near 720 cm^{-1} attributed to CH_2 rocking of alkyl chains containing four or more methylenes in sequence [163], [163], [164]. These assignments are consistent with published reference spectra for UHMWPE and confirm that the bulk polymer chemistry of the substrate is preserved across all treatment conditions.

Figure 4.1 presents reference spectra of functionalized and neat polyethylene, which illustrate the spectral signatures expected from surface functionalization. The treated sample shows a prominent C=O stretching band near 1715 cm^{-1} rising to approximately half the intensity of the dominant C–H stretches, along with a broad O–H stretching band centered around 3300–3400 cm^{-1} and additional C–O features in the 1200–1100 cm^{-1} region [165], [166]. In contrast, the neat polyethylene reference shows only the characteristic CH_2 stretching, bending, and rocking bands described above.

Across the full spectral range of the treated samples, the five plasma treatment conditions produced spectra that are largely indistinguishable from one another. The overlay of all five treated spectra is presented in **Figure 4.2.** No sharp, well-defined absorption peak was observed at 1715 cm^{-1} in any sample, and no pronounced O–H band developed in the 3200–3600 cm^{-1} region The main observation is that bulk polyethylene dominates every trace regardless of

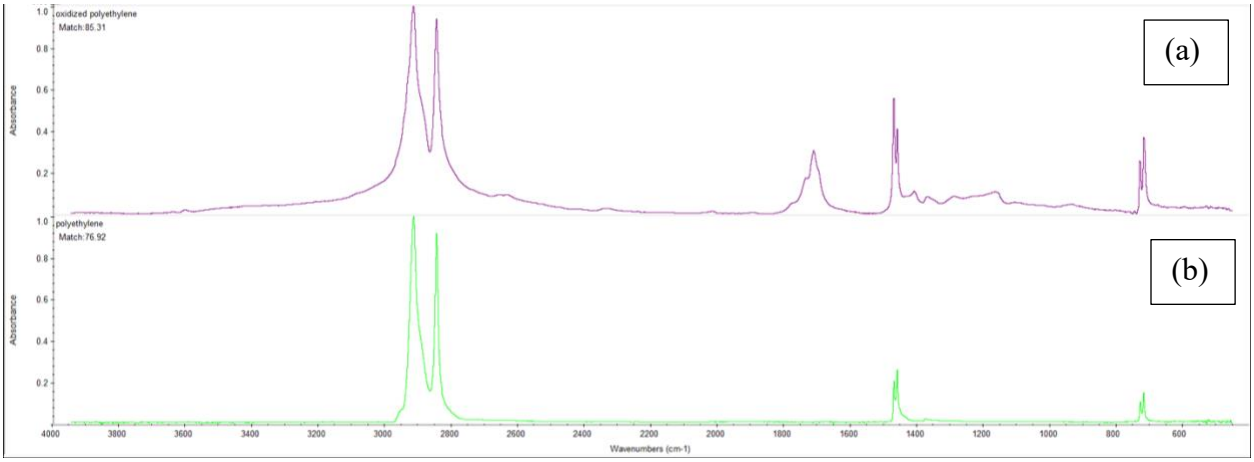


Figure 4.1. Reference FTIR spectra of (a) functionalized and (b) neat polyethylene

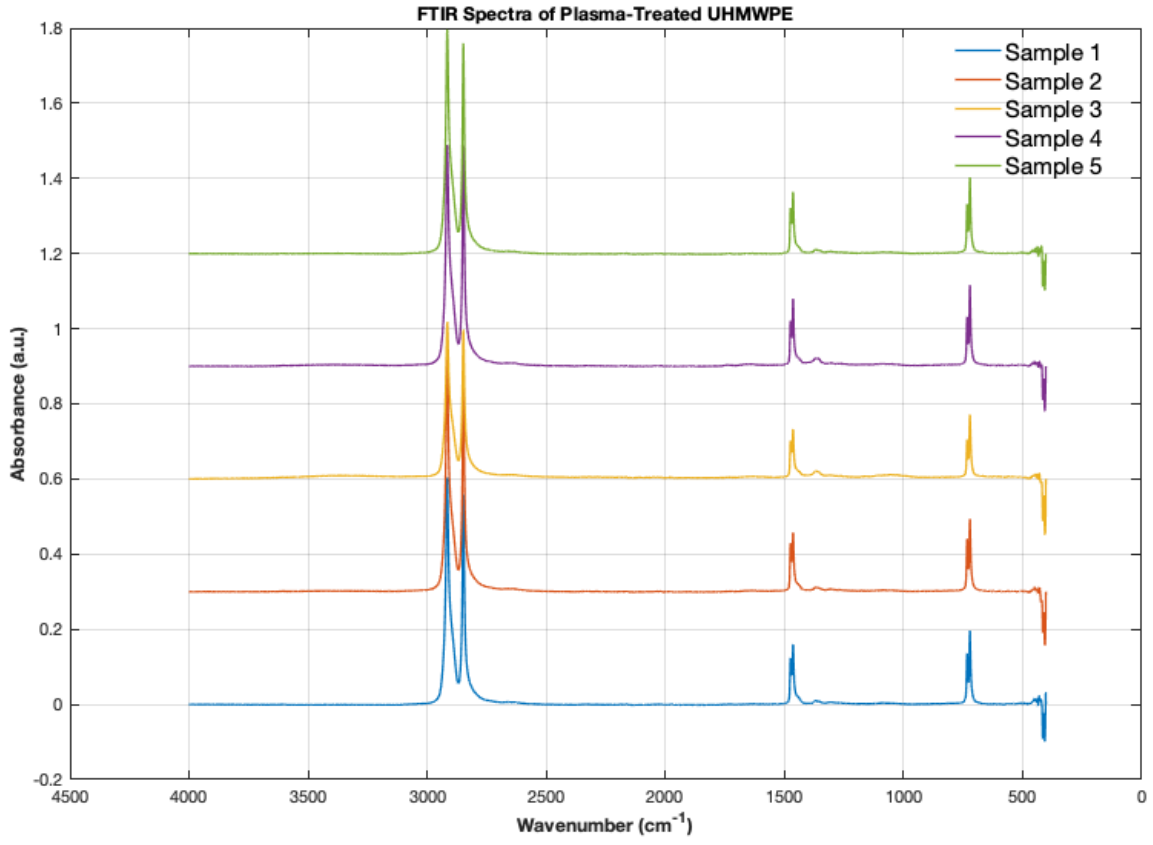


Figure 4.2. Overlay of ATR-FTIR spectra for Samples 1–5 with a vertical offset of 0.3.

plasma treatment speed. Closer inspection did reveal subtle differences in Sample 3. A small but consistent elevation in absorbance in the 3600–3200 cm^{-1} region is observed compared to the other samples. This is the region where O–H stretching vibrations are typically found [159], [165]. Another minor absorbance increase in the 1700–1600 cm^{-1} region, where C=O and C=C stretches are expected [160], [166], was also observed. These deviations are very small in magnitude, on the order of 0.005–0.010 absorbance units above the baseline of the other samples. No discrete peak was observed at 1715 cm^{-1} either. The functionalized polyethylene reference shows a C=O band on the order of 50% of the intensity of the C–H stretches, whereas the feature observed in Sample 3 is much smaller. Additional variation between samples was observed in the CH_2 bending region near 1450 cm^{-1}, with Samples 2 and 3 showing a modest increase in relative absorbance compared to the other samples. This variation did not correlate proportionally with treatment speed. The deviations observed in Sample 3 are therefore best described as suggestive trends rather than definitive identification of oxygen-containing functional groups.

Water Contact Angle

Water contact angle (WCA) measurements were used to assess changes in free surface energy and in this case, wettability induced by the plasma treatment. The neat, untreated UHMWPE control exhibited a contact angle of 102.7°, consistent with the hydrophobic character of non-polar polyethylene reported in the literature [167]. The same five samples evaluated under FTIR were tested for WCA immediately after absorbance was collected. All five plasma-treated samples exhibited reduced contact angles relative to the untreated control, confirming that the plasma treatment produced a measurable and reproducible increase in surface energy regardless of treatment speed. The only samples that were tested for WCA were samples 1, 2, and 3. This

was because of the little variance shown in the FTIR spectrum, a representative sample from slow, fast, and baseline traverse speeds were chosen. The measured values for each treatment condition are summarized in **Table 4.1**, and a representative sessile-drop image for the untreated sample is shown in **Figure 4.3.**

The lowest contact angle measured was 90.8° on Sample 1 (treated at 1 in/s), corresponding to a reduction of 11.9° relative to the untreated control. Sample 3 (treated at 2.08 in/s, the same traverse speed used in composite fabrication) produced a contact angle of 93.2°, a smaller reduction of 9.5° relative to the untreated control. The reduction in contact angle for every treated sample, is counterintuitive compared to the FTIR spectra.

The apparent discrepancy between the two techniques is resolved by recognizing a fundamental limitation of ATR-FTIR as a characterization technique for plasma-treated polymer surfaces. Atmospheric plasma treatment of polyethylene modifies only a very thin region of the surface, with reported oxidation depths on the order of a few tens of nanometers for typical plasma processes and up to approximately 120 nm for more energetic treatment [160], [161]. The plasma species do not penetrate deeply into the bulk polymer, and the chemical changes they induce are confined to this shallow layer [160], [78]. ATR-FTIR, in contrast, probes the sample

Table 4.1. Water contact angle by plasma treatment speed**.**

Sample	Traverse Speed (in/s)	Contact Angle (°)	Δ vs. Control (°)
Control (neat)	–	102.7	–
Sample 1	1.00	90.8	- 11.9
Sample 3	2.08	93.2	- 9.5
Sample 5	3.03	101.1	- 1.6

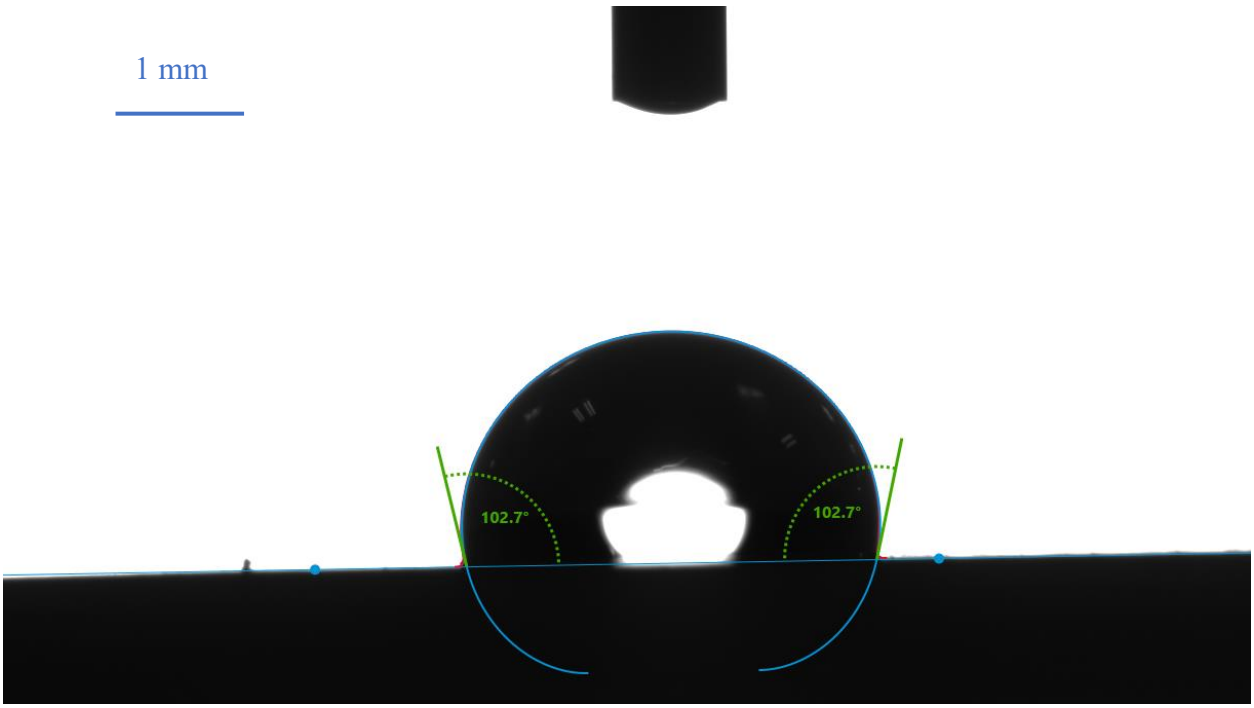


Figure 4.3. Representative sessile-drop image of a water droplet on untreated UHMWPE

via an evanescent wave with a penetration depth of approximately 0.5–2 μm, depending on the ATR crystal material, angle of incidence, and wavenumber of interest [168], [169]. [170]. Therefore, the signal recorded in each spectrum is overwhelmingly dominated by the underlying unmodified bulk UHMWPE, and any new functional groups present on the true surface contribute only a small fraction of the total absorbance. Wettability is governed by the outermost few molecular layers of a surface, because the interaction between a water droplet and the substrate occurs at the solid–liquid interface and depends on the density and orientation of polar groups directly exposed to the probe liquid [171], [172]. The WCA results therefore provide the primary evidence of successful surface modification in this study, with the FTIR spectra serving as confirmation that the bulk polymer was not significantly disturbed.

The relationship between treatment speed and contact angle is linear within the range tested. As plasma dwell time increases, the water contact angle decreases. Sample 5, which received the shortest plasma dwell time at 3.03 in/s, produced a contact angle of only 101.1°. This is 1.6° below the untreated control (102.7°) and well within the range in which treatment can be said to be effectively minimal. Sample 3, treated at the intermediate speed of 2.08 in/s, produced a contact angle of 93.2°. This is a reduction of 9.5° relative to the control and 7.9° relative to sample 5. Sample 1, treated at the slowest speed of 1.00 in/s, receiving roughly three times the plasma dwell time of Sample 5, produced the lowest contact angle of 90.8°. This is a reduction of 11.9° relative to the control and of 10.3° relative to sample 5. These results are consistent with the expected behavior for atmospheric plasma activation of a hydrophobic polyolefin surface. The longer exposure delivers a larger flux of reactive species to the surface and therefore creates a higher areal density of polar functional groups, leading to a more wettable surface [160], [165], [78]. The reduction achieved between Sample 3 and Sample 1 (2.4°) is

notably smaller than that between Sample 5 and Sample 3 (7.9°). This suggests that the productive effect of additional dwell time is already beginning to taper at the 2.08 in/s condition, even though no net regression has set in within the range of speeds tested here.

Although Sample 1 produced the lowest contact angle of the five speeds evaluated on neat UHMWPE films, the 2.08 in/s traverse speed used for Sample 3 was selected for composite fabrication. This selection was made because the CF/UHMWPE nonwoven plies are susceptible to localized melting and charring at traverse speeds below 2.08 in/s. This speed represents the most aggressive plasma treatment compatible with the composite substrate, rather than the absolute optimum on a flat film. The 9.5° WCA reduction achieved at this speed is sufficient to confirm that successful surface activation was delivered to the composite plies used in Variants CP and CPD, without inducing thermal damage to the UHMWPE component.

The observation that Sample 3 was also the sample in which a small but consistent elevation in absorbance was visible in the 3600–3200 cm^{-1} (O–H stretch) and 1700–1600 cm^{-1} (C=O / C=C stretch) regions of the ATR-FTIR spectrum further supports the interpretation that the 2.08 in/s condition delivers meaningful polar-group incorporation, even though the absolute depth of modification is too shallow to be resolved quantitatively by ATR-FTIR.

Three-Point Bend Fatigue Test

Three-point bend fatigue testing was performed on all four composite variants in both virgin and healed states to characterize fatigue life and quantify the effectiveness of the healing process. Three fatigue curves were collected for each variant in each state, and the healed curves were overlaid onto the virgin curves for direct visual comparison. The results for variants CN and CPD are presented in **Figure 4.4** and **Figure 4.5.** A logarithmic decay-rate analysis of all the

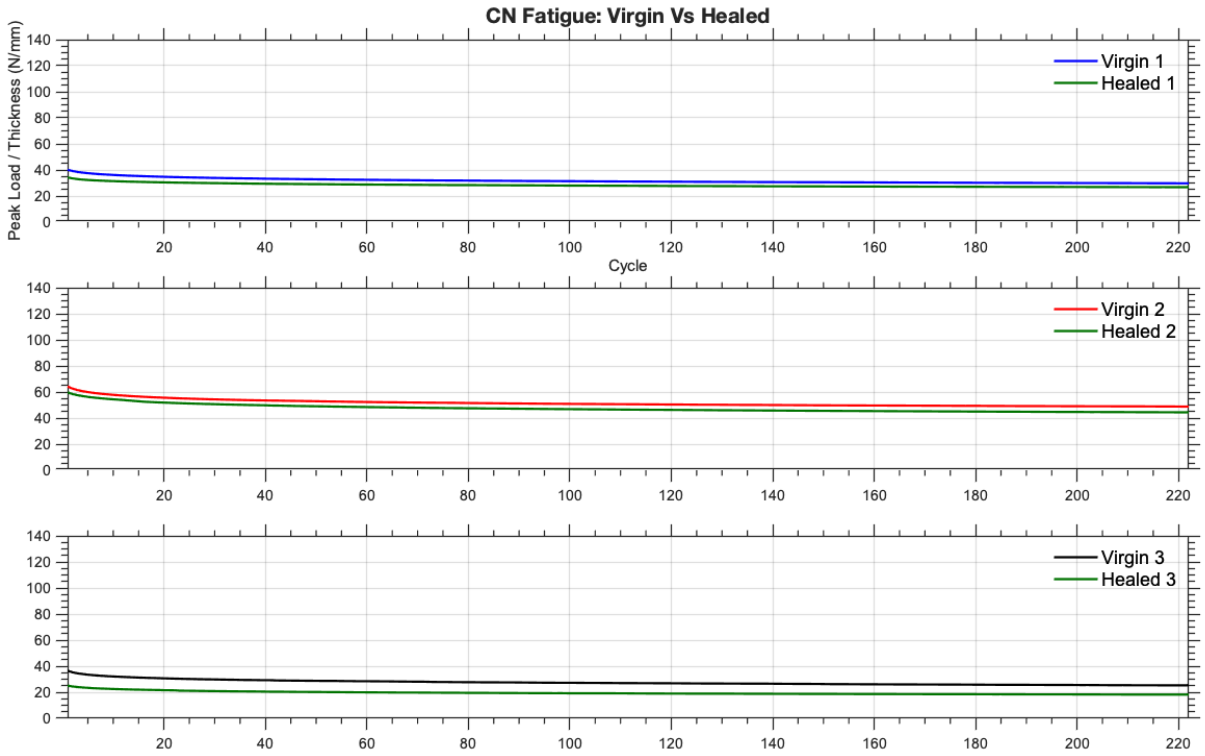


Figure 4.4. Full fatigue curves over 223 cycles for CN samples 1, 2, and 3. All curves have been normalized by the thickness of each sample.

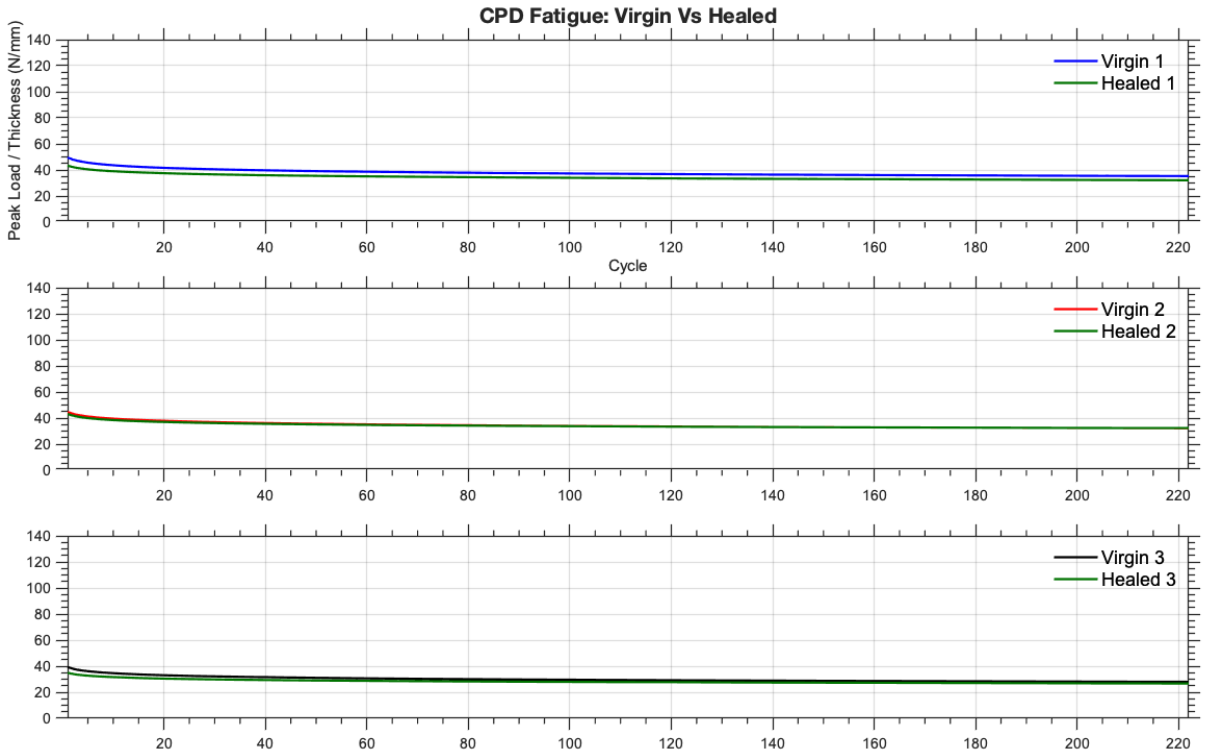


Figure 4.5. Full fatigue curves over 223 cycles for CPD samples 1, 2, and 3. All curves have been normalized by the thickness of each sample.

variants is shown in **Table 4.2**. The full-curve healing efficiency calculation based on the area under the fatigue curves is shown in **Figure 4.6**. These results directly evaluate the functional recovery of mechanical performance after damage and healing and provide the most mechanically meaningful measure of healing performance in this study.

Visual inspection of the fatigue curves reveals qualitative differences between the variants. In the CPD variant, the healed fatigue curves lie almost directly on top of the virgin curves across the full fatigue curve. By contrast, in the CN variant there is a clear and persistent gap between the healed and virgin curves, with the healed curves lying consistently below the virgin curves. This qualitative difference is the single most visually striking feature of the fatigue dataset and previews the quantitative differences captured by the decay-rate and healing-efficiency analyses that follow.

Each fatigue curve was fit with a logarithmic decay function, and the resulting decay rates are arranged in **Table 4.2**. All fits achieved excellent correlation coefficients ($R^2 \geq 0.998$), indicating that the logarithmic decay model is a good description of the fatigue behavior across all variants and states. The healed samples exhibit less negative decay rates than their virgin counterparts in every variant, indicating a slower rate of fatigue-induced property degradation in the healed state. The percentage change in decay rate between virgin and healed varies substantially across variants, from 16% for CN to 37.1% for CP. This variation is discussed alongside the healing efficiency results below.

A full-curve healing efficiency was calculated for each variant based on the relationship between the healed and virgin fatigue curves using **Equation 3.3**. The CPD variant achieved the highest healing efficiency of 94.72%, exceeding the other three variants by a margin of at least seven percentage points. The CN variant, while achieving a mean healing efficiency of 83.94%,

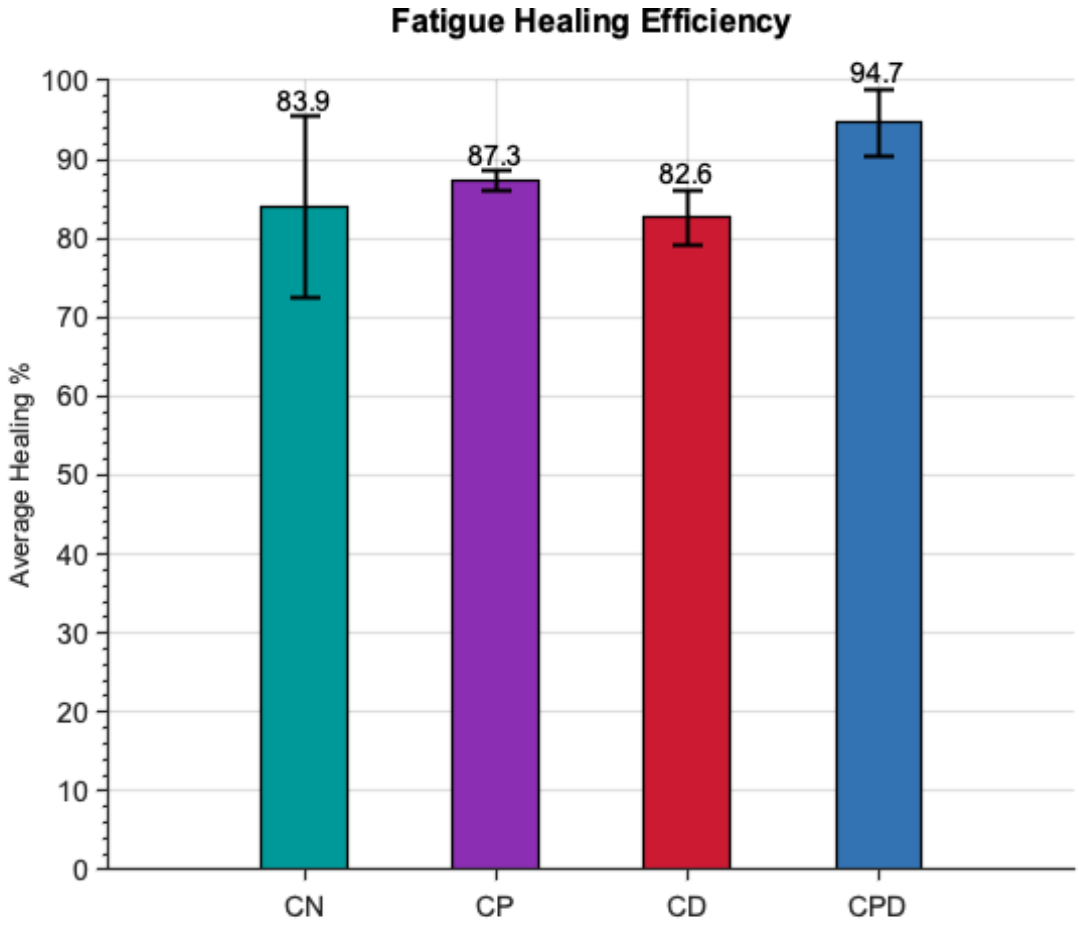


Figure 4.6. Full fatigue curve healing efficiency over 223 cycles for all variants.

Table 4.2. Logarithmic decay-rate analysis of fatigue curves for all four variants in virgin and healed states.

Variant	Virgin Decay Rate	Healed Decay Rate	% Change	Avg R^2
CN	-2.36 ± 0.45	-1.99 ± 0.97	16	0.998
CP	-2.03 ± 0.66	-1.28 ± 0.48	37.1	0.998
CD	-1.64 ± 0.24	-1.07 ± 0.14	34.7	0.999
CPD	-2.40 ± 0.27	-1.92± 0.32	20	0.999

exhibited a standard deviation larger than the standard deviations for any of the other variants. This large difference indicates that apparent healing in CN is highly inconsistent from sample to sample, whereas healing in the treated variants is highly reproducible.

The CPD variant exhibits the highest and most consistent healing performance, and it is closely supported by the visual observation that the healed CPD fatigue curves overlay the virgin curves across the fatigue test and XCT data/analysis. This result is consistent with the interpretation developed across the preceding sections: in CPD, the plasma treatment activates the UHMWPE fiber surfaces, and the disulfide interfacial material bonds to these activated surfaces and remains localized at the ply interfaces. Because the disulfide is positioned at the interface, it is exactly where delamination damage occurs during fatigue loading, and its dynamic covalent bonds are available to re-form across the damaged interface during thermal healing.

The CD variant demonstrates that 4-APD alone produces only partial healing and at the cost of bulk stiffness. CD achieved a healing efficiency of 82.61%, a decay-rate reduction of 34.7%, and the lowest storage modulus of any variant (4.05 GPa). These three observations can be explained by the lack of polar functional groups present during composite consolidation.

Without plasma-generated polar functional groups at sufficient density on the CF/UHMWPE surfaces, the primary amines of 4-APD have no meaningful population of reactive partners with which to form covalent bonds. While untreated carbon fiber surfaces carry residual oxygen-containing functionalities from manufacturing and processing [173], their density on a CF/UHMWPE nonwoven ply is insufficient to anchor the 4-APD coating across the interply area. This causes the 4-APD to remain as a physically absorbed deposit on the ply surfaces rather than as a chemically anchored interlayer. During the 160 °C, 5000 lb consolidation cycle, the coating melts and is free to flow into the bulk of the composite, driven by the large pressure differential across the stack and the open porosity of the partially consolidated plies. This migration has two simultaneous consequences. First, the 4-APD is now distributed throughout the bulk and acts as a plasticizer in the composite. This softens the composite and reduces its storage modulus [174]. Second, the 4-APD is no longer localized at the ply interfaces and cannot effectively re bind the delaminated interface. The healing observed in CD is not interfacial healing but rather generalized disulfide exchange occurring with whatever 4-APD happens to remain near a fatigue-damaged region. This proves to be a far less efficient process than the interfacial mechanism realized in CPD.

The CP variant shows strong decay-rate improvement but lacks a healing mechanism at delamination sites. The CP variant exhibits the largest decay-rate change (37.1%) and an average healing efficiency of 87.35%. This is initially surprising, as plasma treatment alone does not introduce capability of re-forming bonds across interfaces. The observed healing in CP is therefore not true chemical healing but rather a combination of thermal relaxation of residual stresses during the heal cycle and the natural recovery of deformation at elevated temperature. The apparent healing in CP is real but mechanistically distinct from that of CPD, and it would

not be expected to persist over multiple damage–heal cycles. The disulfide-based mechanism in CPD should in principle support repeated healing cycles, though this is beyond the scope of the present study.

The CN variant shows high variance, consistent with its lack of any engineered healing mechanism. The CN healing efficiency is the most variable of the four variants. CN contains no plasma treatment and no disulfide, so any healing observed is attributable to uncontrolled processes. This includes residual stress relaxation, viscoelastic recovery, and sample-to-sample differences in damage morphology and ply packing. The very large standard deviation demonstrates that in the absence of a designed healing mechanism, the apparent recovery of fatigue performance is dominated by natural variation in the composite. Nonwoven composites are known to exhibit inherent variability due to non-uniform fiber distribution and heterogeneous ply packing [26], [175], and this variability dominates the CN healing response. Some of the sample-to-sample variance in all four variants can be attributed to this natural variance, but its disproportionate effect on CN is diagnostic of the absence of a controlled healing mechanism. The CN samples were also observed to deform more during fatigue than the other variants. The CN samples retained some of their observed deformations even after the healing cycle.

X-Ray Computed Tomography

X-ray computed tomography (XCT) was used to non-destructively visualize and quantify internal damage and subsequent healing in the composite samples. XCT was performed on representative samples of the CN and CPD variants at three states: undamaged, damaged, and healed. The same slice location was extracted from each reconstruction to allow direct visual comparison across the three states. Void content was quantified for each stage as a volumetric percentage of the whole sample's reconstructed volume. Representative CT slices for the CN and

CPD samples at each stage are shown in **Figure 4.7** and **Figure 4.8**, and the quantified void contents are reported in **Table 4.3.**

Table 4.3. Void content from X-ray CT analysis of CN and CPD variants at three states.

Variant	Undamaged (%)	Damaged (%)	Healed (%)	Δ Undamaged → Healed
CN	12.85	16.39	15.26	+18.8%
CPD	10.62	11.58	10.96	+3.2%

The CN variant exhibited a substantially higher baseline void content (12.85%) than the CPD variant (10.62%) in the undamaged state. Comparing the undamaged and healed states, the CN variant shows an 18.8% relative increase in void content, while the CPD variant shows only a 3.2% relative increase. These void calculations show a distinct difference in both variants' ability to heal delamination. The CN sample is unable to heal the delamination because there is no 4-APD at the interface. CPD however shows clear ability to recover damage.

Three important differences between the CN and CPD variants can be inferred from the data in **Table 4.3**. First, the lower baseline void content of CPD relative to CN (10.62% versus 12.85% by volume) indicates that the combined plasma and disulfide treatment produces a more compact, better-consolidated laminate than the untreated composite. This is consistent with the role of the plasma treatment in activating the UHMWPE fiber surfaces to promote stronger interfacial adhesion during consolidation [175], [176].

Second, damage accumulation during fatigue is substantially smaller in CPD than in CN. After fatigue, the CN void fraction rose from 12.85% to 16.39%, a 27.55% increase relative to its undamaged baseline. Over the same damage step, the CPD void fraction rose from 10.62% to

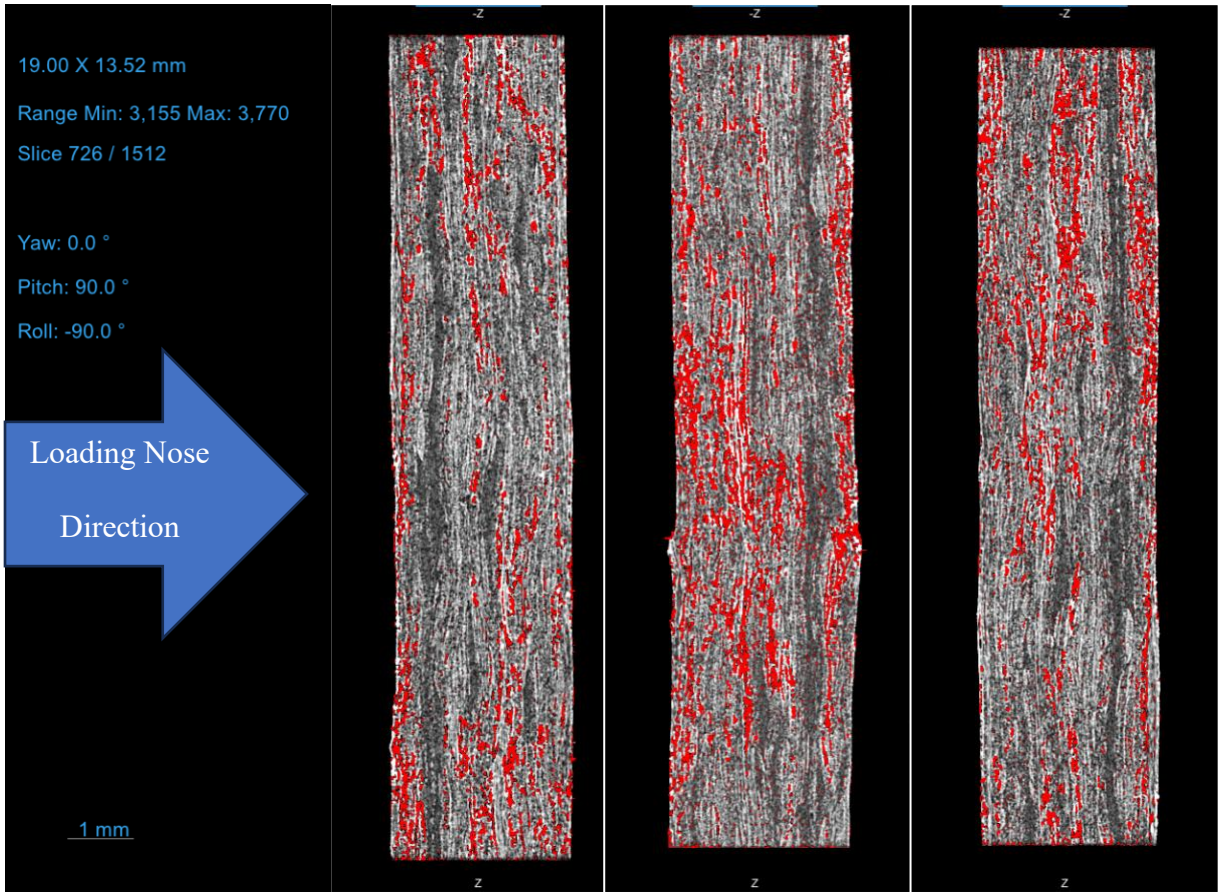


Figure 4.7. X-ray CT images of the CN variant at three different states. (a) Undamaged, (b) damaged, (c) healed. Each image was taken at the same slice over the three states.

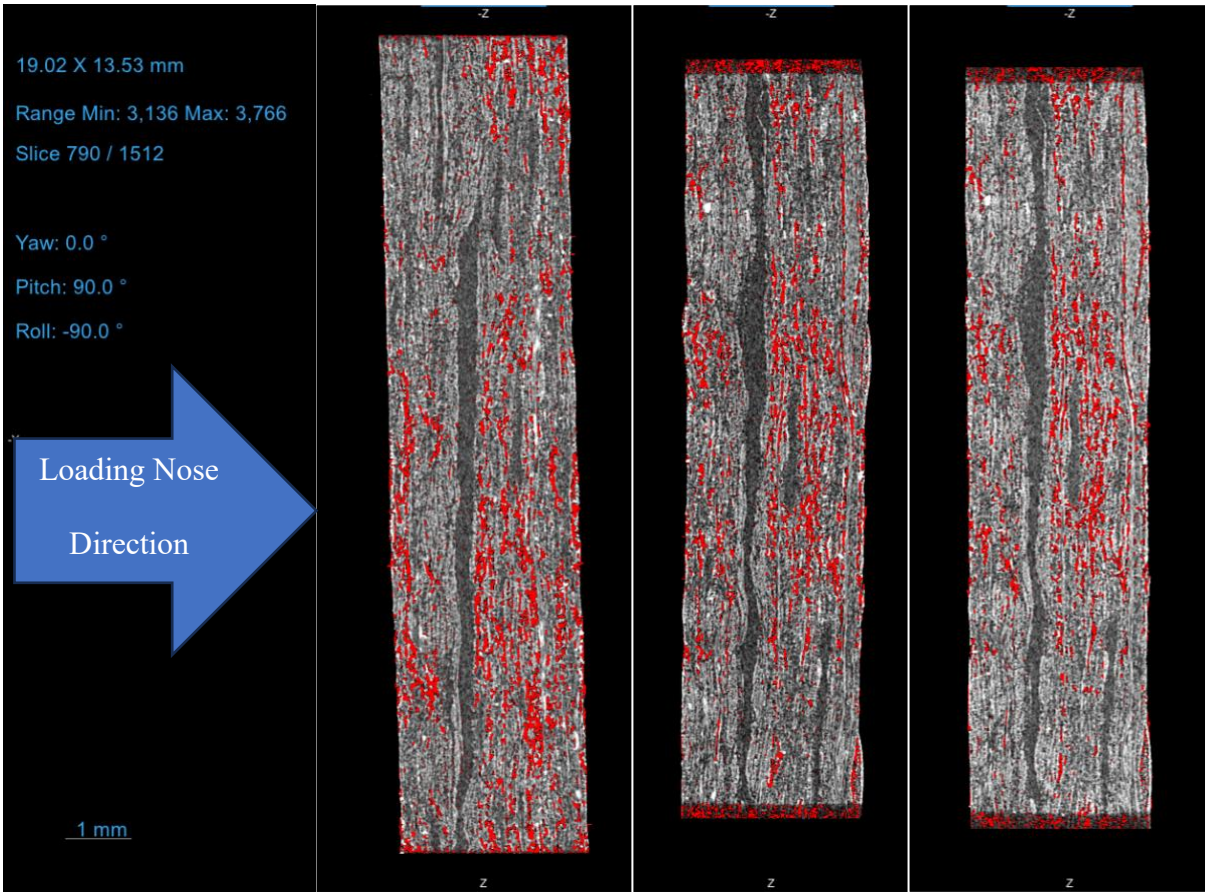


Figure 4.8. X-ray CT images of the CPD variant at three different states. (a) Undamaged, (b) damaged, (c) healed. Each image was taken at the same slice over the three states.

11.58%, only a 9.0% increase relative to its undamaged baseline. CPD accumulated roughly one-third as much internal damage as CN under identical fatigue loading. This improved damage resistance likely comes from two complementary mechanisms. The plasma-activated surfaces distribute stress more uniformly through the laminate rather than concentrating it at weakly bonded ply boundaries [175], [176]. The disulfide interlayer also provides an anchored, homogeneous interply region capable of absorbing and redistributing local stress concentrations.

Third, the recovery response after the healing cycle differs dramatically between the two variants. Measured against each specimen's own undamaged baseline, CPD returned to within 3.2% of its original void content, while CN remained 18.8% above its original void content. This difference in relative recovery is the central quantitative result of the CT analysis and is consistent with the interpretation that CPD possesses a functional healing mechanism localized at the ply interfaces, while CN does not.

Dynamic Mechanical Analysis

Dynamic mechanical analysis was performed on virgin samples of each variant to establish baseline storage modulus values and to assess how each surface and interfacial treatment affects the ambient-temperature stiffness of the composite. Storage modulus values reported throughout this section were extracted at the starting temperature of 25 °C. This was chosen so that the stiffness rankings reflect the performance the laminate delivers at the temperature it is most often used in rather than performance somewhere in its viscoelastic relaxation regime. The mean E′ values for each variant are presented in **Figure 4.9.**

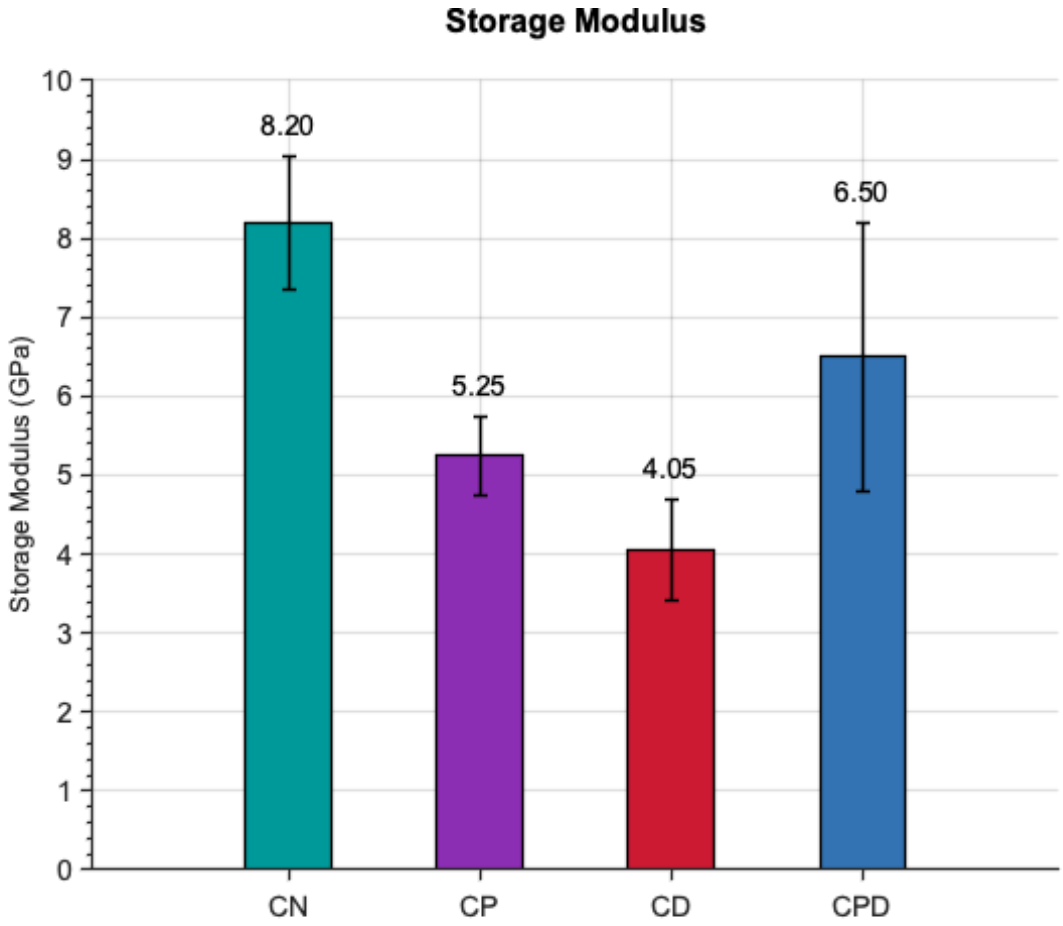


Figure 4.9. Dynamic mechanical analysis storage modulus values for each variant at 25°C.

The CN variant exhibited the highest storage modulus of the four variants, with an average value of 8.2 GPa at 25 °C. The introduction of plasma treatment alone (CP) reduced the storage modulus to 5.35 GPa, and the introduction of disulfide alone (CD) reduced it the furthest to 4.05 GPa. The combined CPD variant recovered a substantial fraction of the lost stiffness relative to CP and CD, returning to an average of 6.5 GPa. These four values reveal a trade-off that is inherent to the surface and interfacial modifications used in this study. The CN variant produces the stiffest composite with no interface modification. Any additional layer or surface modification introduced between the UHMWPE plies alters the stress transfer between fiber layers. A stiff, well-anchored interface transfers load efficiently, while a compliant or heterogeneous interface does not [177].

CD exhibited the lowest modulus of any variant, a 51% reduction relative to CN. This result is consistent with the explanation of the 4-APD coating being distributed throughout the bulk rather than being localized at the ply interfaces. The CP modulus of 5.35 GPa, between CN and CPD, is attributable to process-level effects of the plasma treatment that were observed during composite fabrication. The force of the plasma jet was strong enough to remove loose surface fibers from the plies. This effect locally reduced the areal density of reinforcement available at the interply region. Also, the heat generated by the plasma was sufficient to locally melt previously un-melted UHMWPE fibers at the ply surface. Both effects introduce ply-to-ply heterogeneity that degrades bulk stiffness independent of any chemistry change. Plasma surface activation carries a structural cost that any future optimization of the treatment must address.

CPD recovered to 6.5 GPa, a 60% increase over CD despite containing the same 4-APD coating. This recovery is the strongest stiffness evidence that the 4-APD in CPD remains

anchored at the interface rather than migrating into the bulk. If it migrated, CPD would be expected to show a CD-like reduced modulus regardless of the plasma treatment that preceded it. The plasma activation is therefore acting not only as a chemical anchor for healing but also as a structural anchor that preserves bulk stiffness.

The DMA samples were not subjected to damage–heal cycles and re-tested. The values reported here characterize baseline composite stiffness only and do not characterize modulus recovery after healing; this is identified as a direction for future work in Chapter 5.

CHAPTER FIVE – CONCLUSIONS AND RECOMMENDATIONS

The present work investigated the effect of combined plasma surface activation and disulfide interfacial chemistry on the healing performance of a nonwoven CF/UHMWPE composite. Four composite variants — CN, CP, CD, and CPD — were characterized by FTIR spectroscopy, water contact angle measurement, X-ray computed tomography, dynamic mechanical analysis, and three-point bend fatigue testing. The results collectively support a clear interpretation: the combined plasma-and-disulfide treatment produces a composite in which disulfide bonds are localized at the ply interfaces, enabling efficient and reproducible healing through thermally activated disulfide exchange. In the absence of either treatment, the disulfide either fails to bond (CD) or is never present at the interface (CP, CN), and healing performance degrades accordingly. The following sections combine the main conclusions of each component of this work and provide specific recommendations for further investigation.

Plasma Surface Treatment

The WCA results established that every plasma treatment condition produced a measurable reduction in contact angle relative to the untreated control. This confirmed successful surface activation across the full range of traverse speeds. The relationship between traverse speed and contact angle linear. The intermediate speed of 2.08 in/s produced a contact angle (93.2°), while the slowest speed of 1.00 in/s produced the lowest contact angle (90.8°). Although lower traverse speeds produced smaller WCA on consolidated UHMWPE films, they caused visible thermal damage to the nonwoven plies during preliminary trials and were not viable for composite fabrication. The 2.08 in/s condition was identified as the most aggressive plasma

treatment compatible with CF/UHMWPE nonwoven plies. The 9.5° reduction in WCA achieved at 2.08 in/s confirms successful surface activation of the plies used in Variants CP and CPD.

The FTIR spectra confirmed that bulk polymer chemistry was preserved across all treatment conditions. This demonstrates that plasma treatment does not degrade the bulk UHMWPE beyond a very shallow surface layer. Direct confirmation of the specific functional groups introduced by the plasma treatment was beyond the resolving power of ATR-FTIR in this system and represents a clear opportunity for follow-up characterization by a more surface-sensitive technique.

An important secondary observation during plasma treatment was that the force of the plasma jet physically removed loose surface fibers from the CF/UHMWPE plies, and that the heat of the plasma was sufficient to locally melt un-melted surface fibers. Both effects disrupt ply-to-ply geometric uniformity in the nonwoven material and contribute to the reduced storage modulus observed in the CP variant. This observation identifies a process-level coupling between plasma treatment and composite mechanical properties that is independent of surface chemistry and that must be considered in any future optimization of plasma parameters.

Disulfide Interfacial Chemistry

The DMA and fatigue data together demonstrated that disulfide alone is mechanically and functionally disadvantageous. The CD variant exhibited the lowest storage modulus of any variant tested (4.05 GPa) and a modest healing efficiency of 82.61%. Both observations are explained by the fact that, in the absence of plasma-introduced reactive sites on the fiber surfaces, the disulfide coating has nothing to bond to and migrates into the bulk during consolidation. Once distributed in the bulk, the disulfide plasticizes the composite globally and is no longer available at the ply interfaces. This result emphasizes that disulfide chemistry alone is

insufficient to produce effective interply healing in a nonwoven CF/UHMWPE composite; the disulfide must be localized at the damage site to function as intended.

The Combined CPD Variant

The CPD variant produced the strongest healing performance measured in this study, with a full-curve healing efficiency of 94.72% and healed fatigue curves that overlap the virgin curves rather than lying below them. The CT data show that CPD returned to within 3.2% of its original void content after healing, compared to 18.8% above original for CN. The DMA data show that CPD recovered substantial stiffness (6.5 GPa) relative to CP and CD individually. This indicates that the disulfide remained localized at the interface when plasma activation was present. Taken together, these results support the conclusion that plasma treatment and disulfide chemistry act harmoniously rather than additively. Plasma alone provides improved interfacial adhesion but no healing mechanism. Disulfide alone provides healing chemistry but fails to stay localized at the interface. Only the combined treatment produces a composite in which disulfide bonds are positioned precisely where damage occurs, and only the combined treatment produces healing efficiency approaching the values reported for well-controlled disulfide-based healing systems in the polymer chemistry literature.

Recommendations for Future Work

The present work establishes a clear picture, but it also identifies several directions in which the study could be productively extended. The highest-priority follow-up is surface-sensitive characterization of the plasma-treated UHMWPE. The FTIR results were limited by the mismatch between ATR penetration depth and plasma modification depth. Independent confirmation of the specific functional groups introduced by the plasma treatment would

substantially strengthen the argument presented here. X-ray photoelectron spectroscopy (XPS) probes only the top few nanometers of a surface and is the standard technique for resolving exactly this ambiguity. An XPS study of the treated UHMWPE films would provide direct evidence of the surface chemistry produced by the plasma treatment and of its interaction with the disulfide.

Post-heal DMA and repeated damage–heal cycles represent another important extension. All DMA data reported in this work were collected on virgin samples. A full characterization of modulus recovery would require DMA measurements on samples that have been damaged, healed, and re-measured. More broadly, the disulfide exchange mechanism is in principle reversible and should support repeated damage–heal cycles, but the present work characterized only a single cycle. A multi-cycle study would test the durability of the CPD healing response and distinguish true chemical healing from physical relaxation.

Optimization of the disulfide loading and application method is a natural next step for improving the CPD performance. The disulfide in this work was applied as an ethanol solution onto each ply before consolidation. A systematic study varying disulfide concentration, spray mass per ply, and solvent could identify the optimum loading for maximum healing efficiency without excessive plasticization. Such a study would also clarify whether the 94.72% healing efficiency observed in CPD represents an optimum or whether further improvement is accessible.

Finally, plasma activation produces chemical anchor points that localize a dynamic covalent healing agent at ply interfaces. The approach could be extended to other polyolefin or other thermoplastic nonwoven systems, and to other classes of dynamic covalent chemistry. Such an extension would test the generality of the mechanism and potentially identify systems in which higher baseline mechanical properties can be retained alongside efficient healing.

Closing Remark

The healing efficiency of 94.72% achieved in the CPD variant, demonstrates that the combination of plasma surface activation and disulfide interfacial chemistry is a viable route to self-healing in high-performance fiber-reinforced composites. The principal contribution of the present work is not the healing efficiency itself but rather the whole picture supported by the full set of five characterization techniques: plasma alone is insufficient, disulfide alone is insufficient, and only their combination produces a composite in which the healing chemistry is positioned precisely where damage occurs. This mechanism provides a design principle that should generalize to other composite systems and other healing chemistries.

REFERENCES

[1] Soutis, C. (2005). Carbon fiber reinforced plastics in aircraft construction. *Materials Science and Engineering: A, International Conference on Recent Advances in Composite Materials*, *412*(1), 171–176. https://doi.org/10.1016/j.msea.2005.08.064.

[2] *Composites Market Report 2023-2028 [499 Pages & 487 Tables]*. (2022). MarketsandMarkets. https://www.marketsandmarkets.com/Market-Reports/composite-market-200051282.html

[3] Abrate, S. (1998). *Impact on Composite Structures*. Cambridge University Press. https://doi.org/10.1017/CBO9780511574504.

[4] Katunin, A. (2019). Criticality of the Self-Heating Effect in Polymers and Polymer Matrix Composites during Fatigue, and Their Application in Non-Destructive Testing. *Polymers*, *11*(1), 19. https://doi.org/10.3390/polym11010019.

[5] Hodge, A. (2007). Damage Tolerance of Composites. *National Space & Missile Materials Symposium*. https://ntrs.nasa.gov/api/citations/20070031963/downloads/20070031963.pdf.

[6] Egbo, M. K. (2021). A fundamental review on composite materials and some of their applications in biomedical engineering. *Journal of King Saud University - Engineering Sciences*, *33*(8), 557–568. https://doi.org/10.1016/j.jksues.2020.07.007.

[7] Ashebir, D. A., Mengesha, G. A., & Sinha, D. K. (2022). An Insight into Mechanical and Metallurgical Behavior of Hybrid Reinforced Aluminum Metal Matrix Composite. *Advances in Materials Science and Engineering*, *2022*(1), 7843981. https://doi.org/10.1155/2022/7843981.

[8] Mallick, P. K. (2007). *Fiber-Reinforced Composites: Materials, Manufacturing, and Design, Third Edition* (3rd ed.). CRC Press. https://doi.org/10.1201/9781420005981.

[9] Matiti, S. (2022). Sustainable Fiber-Reinforced Composites: A Review. *Advanced Sustainable Systems 2022*(6), 2200258. https://doi.org/10.1002/adsu.202200258.

[10] Abbood, I. S. (2021). Properties evaluation of fiber reinforced polymers and their constituent materials used in structures—A review. *Materials Today: Proceedings*. https://doi.org/10.1016/J.MATPR.2020.07.636.

[11] Wang, A., Li, R., & Liu, X. (2024). Analysis of the Tensile Properties and Probabilistic Characteristics of Large-Tow Carbon Fiber-Reinforced Polymer Composites. *Polymers*, *16*(15), 2197. https://doi.org/10.3390/polym16152197.

[12] Davidson, M., Graunke, R., Green, A., Haelsig, H., Heinemann, L., Antony Jose, S., & Menezes, P. L. (2026). Carbon Fiber-Reinforced Polymer Matrix Composites: Processing, Properties, and Applications. *Fibers*, *14*(3), 29. https://doi.org/10.3390/fib14030029.

[13] Ashby, M. F. (2016). *Materials Selection in Mechanical Design*. Butterworth-Heinemann.

[14] Campbell, F. C. (2010). *Structural Composite Materials*. ASM International. https://doi.org/10.31399/asm.tb.scm.9781627083140.

[15] Gibson, R. F. (2014). A review of recent research on nanoindentation of polymer composites and their constituents. *Composites Science and Technology*, *105*, 51–65. https://doi.org/10.1016/j.compscitech.2014.09.016.

[16] Long natural fibre composites. (2017). In *Advanced High Strength Natural Fibre Composites in Construction* (pp. 141–177). Woodhead Publishing. https://doi.org/10.1016/B978-0-08-100411-1.00006-6.

[17] Odian, G. G. (2004). *Principles of Polymerization* (4th ed.). Wiley. https://doi.org/10.1002/047147875X.

[18] *Knovel—4. Material Property Charts*. (n.d.). Retrieved April 12, 2026, from https://app-knovel-com.utk.idm.oclc.org/kn/resources/kt008C7P92/kpMSMDE022/pdf?b-toc-cid=kpMSMDE022&b-toc-root-slug=materials-selection-in&b-toc-

title=Materials%20Selection%20in%20Mechanical%20Design%20%284th%20Edition%29&b-toc-url-slug=introduction&kpromoter=federation.

[19] Periasamy, K., Kandare, E., Das, R., Darouie, M., & Khatibi, A. A. (2023). Interfacial Engineering Methods in Thermoplastic Composites: An Overview. *Polymers*, *15*(2), 415. https://doi.org/10.3390/polym15020415.

[20] Young, R. J., & Lovell, P. A. (2011). *Introduction to Polymers* (3rd ed.). CRC Press. https://doi.org/10.1201/9781439894156.

[21] Cogswell, F. N. (1992). *Thermoplastic Aromatic Polymer Composites: A Study of the Structure, Processing, and Properties of Carbon Fibre Reinforced Polyetheretherketone and Related Materials*. Butterworth-Heinemann.

[22] Jin, Y., Lei, Z., Taynton, P., Huang, S., & Zhang, W. (2019). Malleable and Recyclable Thermosets: The Next Generation of Plastics. *Matter*, *1*(6), 1456–1493. https://doi.org/10.1016/j.matt.2019.09.004.

[23] Mccauley, M. (2019). Contemporary Methods for Repairing Composite Materials. *DSIAC*. https://dsiac.dtic.mil/articles/contemporary-methods-for-repairing-composite-materials/.

[24] Reis, J. P., de Moura, M., & Samborski, S. (2020). Thermoplastic Composites and Their Promising Applications in Joining and Repair Composites Structures: A Review. *Materials*, *13*(24), 5832. https://doi.org/10.3390/ma13245832.

[25] Advani, S., & Hsiao, K.-T. (2012). *Manufacturing Techniques for Polymer Matrix Composites (PMCs)*. Woodhead.

[26] Maisha I Alam, Kazi M Maraz, & Ruhul A Khan. (2022). A Review on the Application of High-Performance Fiber-Reinforced Polymer Composite Materials. *GSC Advanced Research and Reviews*, *10*(2), 020–036. https://doi.org/10.30574/gscarr.2022.10.2.0036.

[27] Melito, S. (2022, November 9). *Thermoplastics vs. Thermoset Plastics | Material Properties | Fictiv*. https://www.fictiv.com/articles/thermoplastic-vs-thermoset-plastic-mechanical-properties-overview.

[28] Nazarenko, L., Stolarski, H., & Altenbach, H. (2018). Thermo-elastic properties of random composites with unidirectional anisotropic short-fibers and interphases. *European Journal of Mechanics - A/Solids*, *70*, 249–266. https://doi.org/10.1016/j.euromechsol.2018.01.002.

[29] López-Santos, F., May-Pat, A., Ledesma-Orozco, E., Hernández-Pérez, A., & Avilés, F. (2021). Measurement of in-plane and out-of-plane elastic properties of woven fabric composites using digital image correlation. *Journal of Composite Materials*, *55*(9), 1231–1246. https://doi.org/10.1177/0021998320967073.

[30] Chowdhury, I. R., & Summerscales, J. (2024). Woven Fabrics for Composite Reinforcement: A Review. *Journal of Composites Science*, *8*(7), 280. https://doi.org/10.3390/jcs8070280.

[31] Kashani, M. H., & Milani, A. S. (2016). Damage Prediction in Woven and Non-woven Fabric Composites. In *Non-woven Fabrics*. IntechOpen. https://doi.org/10.5772/61511.

[32] Månson, V. M., J. A. E. (2001). Impregnation of Compressible Fiber Mats with a Thermoplastic Resin. Part I: Theory - V. Michaud, J. -A. E. Månson, 2001. *Journal of Composite Materials*. https://journals.sagepub.com/doi/epdf/10.1177/002199801772662271.

[33] Liu, J., Li, C., Yang, Y., Wang, W., Guo, F., Jing, K., & Wang, L. (2025). Ultra-high Molecular Weight Polyethylene: From Synthesis to Applications. *Journal of Organometallic Chemistry*, *1042*, 123870. https://doi.org/10.1016/j.jorganchem.2025.123870.

[34] Wang, H., Cheng, P., Lei, M., Han, Z., Li, G., & Chen, Y. (2026). A Review on the Mechanical Properties of Continuous Fiber-Reinforced Composites Fabricated by Conventional

and Additive Manufacturing. *Composites Part A: Applied Science and Manufacturing*, *206*, 109755. https://doi.org/10.1016/j.compositesa.2026.109755.

[35] Phiri, R., Mavinkere Rangappa, S., Siengchin, S., Oladijo, O. P., & Ozbakkaloglu, T. (2024). Advances in Lightweight Composite Structures and Manufacturing Technologies: A Comprehensive Review. *Heliyon*, *10*(21), e39661. https://doi.org/10.1016/j.heliyon.2024.e39661.

[36] Jin, Z., Han, Z., Chang, C., Sun, S., & Fu, H. (2022). Review of Methods for Enhancing Interlaminar Mechanical Properties of Fiber-Reinforced Thermoplastic Composites: Interfacial Modification, Nano-Filling and Forming Technology. *Composites Science and Technology*, *228*, 109660. https://doi.org/10.1016/j.compscitech.2022.109660.

[37] Tamuzs, V., Tarasovs, S., & Vilks, U. (2003). Delamination Properties of Translaminar-Reinforced Composites. *Composites Science and Technology*, *63*(10), 1423–1431. https://doi.org/10.1016/S0266-3538(03)00042-3.

[38] Tay, T. (2003). Characterization and analysis of delamination fracture in composites: An overview of developments from 1990 to 2001. *Applied Mechanics Reviews*, *56*(1), 1–32. https://doi.org/10.1115/1.1504848.

[39] Pagano, N. J., & Pipes, R. B. (1973). Some observations on the interlaminar strength of composite laminates. *International Journal of Mechanical Sciences*, *15*(8), 679–688. https://doi.org/10.1016/0020-7403(73)90099-4.

[40] Wang, J., Potter, K., Hazra, K., & Wisnom, M. (2012). Experimental Fabrication and Characterization of Out-of-Plane Fiber Waviness in Continuous Fiber-Reinforced Composites. *Journal of Composite Materials*, *46*(17), 2041–2053. https://doi.org/10.1177/0021998311429877.

[41] Kim, R. Y., & Pagano, N. J. (1991). Crack Initiation in Unidirectional Brittle-Matrix Composites. *Journal of the American Ceramic Society*, *74*(5), 1082–1090. https://doi.org/10.1111/j.1151-2916.1991.tb04346.x.

[42] Pagano, N. J., & Pipes, R. B. (1973). Some observations on the interlaminar strength of composite laminates. *International Journal of Mechanical Sciences*, *15*(8), 679–688. https://doi.org/10.1016/0020-7403(73)90099-4.

[43] Wisnom, M. R., & Hallett, S. R. (2009). The role of delamination in strength, failure mechanism and hole size effect in open hole tensile tests on quasi-isotropic laminates. *Composites Part A: Applied Science and Manufacturing*, *40*(4), 335–342. https://doi.org/10.1016/j.compositesa.2008.12.013

[44] Joshi, S. C. (2020). Boosting Inter-ply Fracture Toughness Data on Carbon Nanotube-Engineered Carbon Composites for Prognostics. *Journal of Composites Science*, *4*(4). https://doi.org/10.3390/jcs4040170

[45] Nasuha, N., Azmi, A., & Lih, T. (2017). A review on mode-I interlaminar fracture toughness of fibre reinforced composites. *Journal of Physics: Conference Series*, *908*, 012024. https://doi.org/10.1088/1742-6596/908/1/012024.

[46] Benzeggagh, M. L., & Kenane, M. (1996). Measurement of mixed-mode delamination fracture toughness of unidirectional glass/epoxy composites with mixed-mode bending apparatus. *Composites Science and Technology*, *56*(4), 439–449. https://doi.org/10.1016/0266-3538(96)00005-X

[47] Reeder, J., & Crews, Jr., J. (1990). The mixed-mode bending method for delamination testing. In *30th Structures, Structural Dynamics and Materials Conference*. American Institute of Aeronautics and Astronautics. https://doi.org/10.2514/6.1989-1347.

[48] Asp, L., Sjögren, A., & Greenhalgh, E. (2001). Delamination Growth and Thresholds in a Carbon/Epoxy Composite Under Fatigue Loading. *Journal of Composites Technology & Research*, *23*(2), 55–68. https://doi.org/10.1520/CTR10914J.

[49] Tavares, S. M. O., & de Castro, P. M. S. T. (2017). An overview of fatigue in aircraft structures. *Fatigue & Fracture of Engineering Materials & Structures*, *40*(10), 1510–1529. https://doi.org/10.1111/ffe.12631

[50] Katnam, K. B., Da Silva, L. F. M., & Young, T. M. (2013). Bonded repair of composite aircraft structures: A review of scientific challenges and opportunities. *Progress in Aerospace Sciences*, *61*, 26–42. https://doi.org/10.1016/j.paerosci.2013.03.003.

[51] Whittingham, B., Baker, A. A., Harman, A., & Bitton, D. (2009). Micrographic studies on adhesively bonded scarf repairs to thick composite aircraft structure. *Composites Part A: Applied Science and Manufacturing, Special Issue: Repair*, *40*(9), 1419–1432. https://doi.org/10.1016/j.compositesa.2008.12.011

[52] Katnam, K. B., Da Silva, L. F. M., & Young, T. M. (2013). Bonded repair of composite aircraft structures: A review of scientific challenges and opportunities. *Progress in Aerospace Sciences*, *61*, 26–42. https://doi.org/10.1016/j.paerosci.2013.03.003

[53] Tsotsis, T. K. (1998). Long-Term Thermo-Oxidative Aging in Composite Materials: Experimental Methods. *Journal of Composite Materials*, *32*(11), 1115–1135. https://doi.org/10.1177/002199839803201104

[54] Hayes, B. S., Gilbert, E. N., & Seferis, J. C. (2000). Scaling complications of dual temperature cure resin prepreg systems in airplane part manufacture. *Composites Part A: Applied Science and Manufacturing*, *31*(7), 717–725. https://doi.org/10.1016/S1359-835X(00)00012-9

[55] Hart-Smith, L. J. (1976). Bolded Joints in Graphite-Epoxy Composites. *National Aeronautics and Space Administration*. https://ntrs.nasa.gov/api/citations/19770008495/downloads/19770008495.pdf.

[56] Rhead, A. T., Butler, R., Liu, W., & Baker, N. (2012). The influence of surface ply fibre angle on the compressive strength of composite laminates containing delamination. *The Aeronautical Journal*, *116*(1186), 1315–1330. https://doi.org/10.1017/S000192400000765X.

[57] Hager, M. D., Greil, P., Leyens, C., van der Zwaag, S., & Schubert, U. S. (2010). Self-Healing Materials, *Advanced Materials*. https://advanced.onlinelibrary.wiley.com/doi/full/10.1002/adma.201003036?saml_referrer.

[58] Blaiszik, B., Kramer, S., Olugebefola, S., Moore, J., & Sottos, N. (2010). Self-Healing Polymers and Composites. *Annu. Rev. Mater. Res*, *40*, 179–211211. https://doi.org/10.1146/annurev-matsci-070909-104532.

[59] White, S. R., Sottos, N. R., Geubelle, P. H., Moore, J. S., Kessler, M. R., Sriram, S. R., Brown, E. N., & Viswanathan, S. (2001). Autonomic healing of polymer composites. *Nature*, *409*(6822), 794–797. https://doi.org/10.1038/35057232.

[60] Toohey, K. S., Sottos, N. R., Lewis, J. A., Moore, J. S., & White, S. R. (2007). Self-healing materials with microvascular networks. *Nature Materials*, *6*(8), 581–585. https://doi.org/10.1038/nmat1934.

[61] Hamilton, A. R., Sottos, N. R., & White, S. R. (2011). Pressurized vascular systems for self-healing materials. *Journal of The Royal Society Interface*, *9*(70), 1020–1028. https://doi.org/10.1098/rsif.2011.0508.

[62] Kessler, M. R., Sottos, N. R., & White, S. R. (2003). Self-healing structural composite materials. *Composites Part A: Applied Science and Manufacturing*, *34*(8), 743–753. https://doi.org/10.1016/S1359-835X(03)00138-6.

[63] Ravindran, A. R., Ladani, R. B., Kinloch, A. J., Wang, C.-H., & Mouritz, A. P. (2021). Improving the delamination resistance and impact damage tolerance of carbon fibre-epoxy composites using multi-scale fibre toughening. *Composites Part A: Applied Science and Manufacturing*, *150*, 106624. https://doi.org/10.1016/j.compositesa.2021.106624.

[64] Varley, R. J., & Charve, F. (2012). EMAA as a healing agent for mendable high temperature epoxy amine thermosets. *Composites Part A: Applied Science and Manufacturing*, *43*(7), 1073–1080. https://doi.org/10.1016/j.compositesa.2012.01.018.

[65] Snyder, A. D., Phillips, Z. J., Turicek, J. S., Diesendruck, C. E., Nakshatrala, K. B., & Patrick, J. F. (2022). Prolonged in situ self-healing in structural composites via thermo-reversible entanglement. *Nature Communications*, *13*(1), 6511. https://doi.org/10.1038/s41467-022-33936-z.

[66] Bergman, S. D., & Wudl, F. (2008). Mendable polymers. *J. Mater. Chem.*, *18*(1), 41–62. https://doi.org/10.1039/B713953P.

[67] Kloxin, C. J., Scott, T. F., Adzima, B. J., & Bowman, C. N. (2010). Covalent Adaptable Networks (CANs): A Unique Paradigm in Crosslinked Polymers. *Macromolecules*, *43*(6), 2643–2653. https://doi.org/10.1021/ma902596s.

[68] Montarnal, D., Capelot, M., Tournilhac, F., & Leibler, L. (2011). Silica-Like Malleable Materials from Permanent Organic Networks. *Science*, *(34)*(6058). https://www.science.org/doi/10.1126/science.1212648.

[69] Denissen, W., M. Winne, J., & Prez, F. E. D. (2016). Vitrimers: Permanent organic networks with glass-like fluidity. *Chemical Science*, *7*(1), 30–38. https://doi.org/10.1039/C5SC02223A.

[70] Guerre, M., Taplan, C., Winne, J. M., & Prez, F. E. D. (2020). Vitrimers: Directing chemical reactivity to control material properties. *Chemical Science*, *11*(19), 4855–4870. https://doi.org/10.1039/D0SC01069C.

[71] Zheng, J., Lu, J., Yang, Z., & Liu, T. (2024). Fabrication of recyclable and biodegradable PBAT vitrimer via construction of highly dynamic cross-linked network. *Polymer Degradation and Stability*, *219*, 110602. https://doi.org/10.1016/j.polymdegradstab.2023.110602.

[72] Luzuriaga, A. R. de, Martin, R., Markaide, N., Rekondo, A., Cabañero, G., Rodríguez, J., & Odriozola, I. (2016). Epoxy resin with exchangeable disulfide crosslinks to obtain reprocessable, repairable and recyclable fiber-reinforced thermoset composites. *Materials Horizons*, *3*(3), 241–247. https://doi.org/10.1039/C6MH00029K.

[73] Azcune, I., & Odriozola, I. (2016). Aromatic disulfide crosslinks in polymer systems: Self-healing, reprocessability, recyclability and more. *European Polymer Journal*, *84*, 147–160. https://doi.org/10.1016/j.eurpolymj.2016.09.023.

[74] Donnet, J.-B., & Bansal, R. C. (1998). *Carbon Fibers* (3rd ed.). CRC Press. https://doi.org/10.1201/9781482285390.

[75] Pocius, A. V. (1996). *Adhesion and Adhesives Technology: An Introduction*. Hanser Gardner Publications.

[76] Rice, C. G. C., Evans, A., Turner, Z. R., Wattoom, J., & O'Hare, D. (2025). Strategies for enhancing the processability of UHMWPE. *Industrial Chemistry & Materials*, *3*(2), 178–190. https://doi.org/10.1039/D4IM00104D.

[77] Briggs, David., & Beamson, Graham. (1992). Primary and secondary oxygen-induced C1s binding energy shifts in x-ray photoelectron spectroscopy of polymers. *Analytical Chemistry*, *64*(15), 1729–1736. https://doi.org/10.1021/ac00039a018.

[78] Bertin, M., Leitao, E. M., Bickerton, S., Verbeek, C. J. R. (2024). A review of polymer surface modification by cold plasmas toward bulk functionalization. *Plasma Processes and Polymers*. https://onlinelibrary.wiley.com/doi/abs/10.1002/ppap.202300208.

[79] Wang, Y., Pham, D. T., & Ji, C. (2015). Self-healing composites: A review. *Cogent Engineering*, *2*(1), 1075686. https://doi.org/10.1080/23311916.2015.1075686.

[80] Durão, M. L., Nobre, L., Mota, C., Bessa, J., Cunha, F., & Fangueiro, R. (2024). Self-Healing Composites: A Path to Redefining Material Resilience—A Comprehensive Recent Review. *Materials*, *17*(19), 4681. https://doi.org/10.3390/ma17194681.

[81] Islam, S., & Bhat, G. (2021). Progress and challenges in self-healing composite materials. *Materials Advances*, *2*(6), 1896–1926. https://doi.org/10.1039/D0MA00873G.

[82] Kanu, N. J., Gupta, E., Vates, U. K., & Singh, G. K. (2019). Self-healing composites: A state-of-the-art review. *Composites Part A: Applied Science and Manufacturing*, *121*, 474–486. https://doi.org/10.1016/j.compositesa.2019.04.012.

[83] Adil, Md. M., Rabbi, M. S., & Tasnim, T. (2025). Development of microcapsule-based self-healing composite: A critical review on influencing factors of microencapsulation, healing efficiency, thermal stability and application. *Alexandria Engineering Journal*, *122*, 1–17. https://doi.org/10.1016/j.aej.2025.02.092.

[84] Liu, B., Wu, M., Du, W., Jiang, L., Li, H., Wang, L., Li, J., Zuo, D., & Ding, Q. (2023). The Application of Self-Healing Microcapsule Technology in the Field of Cement-Based Materials: A Review and Prospect. *Polymers*, *15*(12). https://doi.org/10.3390/polym15122718.

[85] Jin, H., Mangun, C. L., Stradley, D. S., Moore, J. S., Sottos, N. R., & White, S. R. (2012). Self-healing thermoset using encapsulated epoxy-amine healing chemistry. *Polymer*, *53*(2), 581–587. https://doi.org/10.1016/j.polymer.2011.12.005.

[86] Hia, I. L., Vahedi, V., & Pasbakhsh, P. (2016). Self-Healing Polymer Composites: Prospects, Challenges, and Applications. *Polymer Reviews*, *56*(2), 225–261. https://doi.org/10.1080/15583724.2015.1106555.

[87] Je, P. C., Sultan, M. T., Selvan, C. P., Irulappasamy, S., Mustapha, F., Basri, A. A., & Safri, S. N. A. (2020). Manufacturing challenges in self-healing technology for polymer composites—A review. *Journal of Materials Research and Technology*, *9*(4), 7370–7379. https://doi.org/10.1016/j.jmrt.2020.04.082.

[88] Shields, Y., De Belie, N., Jefferson, A., & Van Tittelboom, K. (2021). A review of vascular networks for self-healing applications. *Smart Materials and Structures*, *30*(6), 063001. https://doi.org/10.1088/1361-665X/abf41d.

[89] Esser-Kahn, A. P., Thakre, P. R., Dong, H., Patrick, J. F., Vlasko-Vlasov, V. K., Sottos, N. R., Moore, J. S., & White, S. R. (2011). Three-dimensional microvascular fiber-reinforced composites. *Advanced Materials*, *23*(32), 3654–3658. https://doi.org/10.1002/adma.201100933.

[90] Qamar, I. P. S., Sottos, N. R., & Trask, R. S. (2020). Grand challenges in the design and manufacture of vascular self-healing. *Multifunctional Materials*, *3*(1), 013001. https://doi.org/10.1088/2399-7532/ab69e2.

[91] Shivakumar, K., Panduranga, R., & Sharpe, M. (2013). *Interleaved Polymer Matrix Composites—A Review*. https://doi.org/10.2514/6.2013-1903.

[92] Zhang, T., & Yasaee, M. (2022). Influence of thermoplastic interleaves and its healing effect on the failure mechanisms of open-hole notched composite laminates. *Composites Science and Technology*, *227*, 109597. https://doi.org/10.1016/j.compscitech.2022.109597.

[93] Khan, T., Irfan, M. S., Cantwell, W. J., & Umer, R. (2022). Crack healing in infusible thermoplastic composite laminates. *Composites Part A: Applied Science and Manufacturing*, *156*, 106896. https://doi.org/10.1016/j.compositesa.2022.106896.

[94] Guo, M., & Liu, L. (2019). Structuring the thermoplastic interleaf with lotus-leaf-like structure and its interlaminar toughening for CFRPs. *Composites Science and Technology*, *183*, 107825. https://doi.org/10.1016/j.compscitech.2019.107825.

[95] Nascimento, A. A. do. (2021). Self-Healing Polymers and Composite Materials. In *Fiber-Reinforced Plastics*. IntechOpen. https://doi.org/10.5772/intechopen.100908.

[96] Meure, S., Wu, D. Y., & Furman, S. (2009). Polyethylene-co-methacrylic acid healing agents for mendable epoxy resins. *Acta Materialia*, *57*(14), 4312–4320. https://doi.org/10.1016/j.actamat.2009.05.032.

[97] Varley, R. J., Craze, D. A., Mouritz, A. P., & Wang, C. H. (2013). Thermoplastic Healing in Epoxy Networks: Exploring Performance and Mechanism of Alternative Healing Agents. *Macromolecular Materials and Engineering*, *298*(11), 1232–1242. https://doi.org/10.1002/mame.201200394.

[98] Pingkarawat, K., Zhang, J., Wang, C., Varley, R., & Mouritz, A. P. (2013). *Healing and toughening of delamination cracks in carbon-epoxy composites using mendable polymer stitching*.

[99] McBride, M. K., Worrell, B. T., Brown, T., Cox, L. M., Sowan, N., Wang, C., Podgorski, M., Martinez, A. M., & Bowman, C. N. (2019). Enabling Applications of Covalent Adaptable

Networks. *Annual Review of Chemical and Biomolecular Engineering*, *10*(Volume 10, 2019), 175–198. https://doi.org/10.1146/annurev-chembioeng-060718-030217.

[100] Krishnakumar, B., Sanka, R. V. S. P., Binder, W. H., Parthasarthy, V., Rana, S., & Karak, N. (2020). Vitrimers: Associative dynamic covalent adaptive networks in thermoset polymers. *Chemical Engineering Journal*, *385*, 123820. https://doi.org/10.1016/j.cej.2019.123820.

[101] Elling, B. R., & Dichtel, W. R. (2020). Reprocessable Cross-Linked Polymer Networks: Are Associative Exchange Mechanisms Desirable? *ACS Central Science*, *6*(9), 1488–1496. https://doi.org/10.1021/acscentsci.0c00567.

[102] Thiessen, M., & Abetz, V. (2021). Influence of the Glass Transition Temperature and the Density of Crosslinking Groups on the Reversibility of Diels-Alder Polymer Networks. *Polymers*, *13*(8), 1189. https://doi.org/10.3390/polym13081189.

[103] Chen, X., Dam, M. A., Ono, K., Mal, A., Shen, H., & Nutt, S. R. (2002). A thermally re-mendable cross-linked polymeric material. *Science, (295)*(5560). https://go-gale-com.utk.idm.oclc.org/ps/i.do?id=GALE%7CA83914653&v=2.1&it=r&sid=summon&aty=ip&u=knox61277&p=OVIC.

[104] Griffini, G., Rigatelli, B., & Turri, S. (2023). Diels-Alder Macromolecular Networks in Recyclable, Repairable and Reprocessable Polymer Composites for the Circular Economy – A Review. *Macromolecular Materials and Engineering*, *308*(11), 2300133. https://doi.org/10.1002/mame.202300133.

[105] Karatrantos, A. V., Couture, O., Hesse, C., & Schmidt, D. F. (2024). Molecular Simulation of Covalent Adaptable Networks and Vitrimers: A Review. *Polymers*, *16*(10), 1373. https://doi.org/10.3390/polym16101373.

[106] Hayashi, M. (2020). Implantation of Recyclability and Healability into Cross-Linked Commercial Polymers by Applying the Vitrimer Concept. *Polymers*, *12*(6), 1322. https://doi.org/10.3390/polym12061322.

[107] Van Zee, N. J., & Nicolaÿ, R. (2020). Vitrimers: Permanently crosslinked polymers with dynamic network topology. *Progress in Polymer Science*, *104*, 101233. https://doi.org/10.1016/j.progpolymsci.2020.101233.

[108] Denissen, W., Rivero, G., Nicolaÿ, R., Leibler, L., Winne, J., & Du Prez, F. (2015). Vinylogous Urethane Vitrimers. *Advanced Functional Materials*, *25*. https://doi.org/10.1002/adfm.201404553.

[109] Röttger, M., Domenech, T., ven der Weegen, R., Breuillac, A., Nicolaÿ, R., & Leibler, L. (2017). High-performance vitrimers from commodity thermoplastics through dioxaborolane metathesis. *Science*, *(356)*(6333). https://www.science.org/doi/10.1126/science.aah5281

[110] Kaur, G., Kumar, P., & Sonne, C. (2024). Synthesis, properties and biomedical perspective on vitrimers – challenges & opportunities. *RSC Applied Interfaces*, *1*(5), 846–867. https://doi.org/10.1039/D4LF00101J.

[111] Jin, S., Oh, D. X., & Park, J. (2026). Dynamic Disulfide Chemistry for Functional Polymers: Self-Healing, Vitrimer Behavior, and Biochemical/Electronic Applications. *ChemSusChem*, *19*(1), e202501023. https://doi.org/10.1002/cssc.202501023.

[112] Schenk, V., Labastie, K., Destarac, M., Olivier, P., & Guerre, M. (2022). Vitrimer composites: Current status and future challenges. *Materials Advances*, *3*(22), 8012–8029. https://doi.org/10.1039/D2MA00654E.

[113] Sharma, H., Rana, S., Singh, P., Hayashi, M., Binder, W. H., Rossegger, E., Kumar, A., & Schlögl, S. (2022). Self-healable fiber-reinforced vitrimer composites: Overview and future prospects. *RSC Advances*, *12*(50), 32569–32582. https://doi.org/10.1039/d2ra05103f

[114] Gao, L., Wang, H., Yao, X., Zheng, Z., Wang, L., Wang, Z., Wang, Y., Zhang, B., Jing, X., & Wu, J. (2025). High-performance epoxy vitrimer from commercial epoxy-anhydride with reprocessable and chemical degradable properties. *Frontiers in Materials*, *12*. https://doi.org/10.3389/fmats.2025.1552713

[115] Chabert, E., Vial, J., Cauchois, J.-P., Mihaluta, M., & Tournilhac, F. (2016). Multiple welding of long fiber epoxy vitrimer composites. *Soft Matter*, *12*(21), 4838–4845. https://doi.org/10.1039/C6SM00257A

[116] Biswal, T., Sahoo, B., & Kalita, K. (2023). Ultrasonic Welding of Glass Fiber Reinforced Vitrimer Composites. *Composites Part A: Applied Science and Manufacturing*. https://doi.org/10.1016/j.compositesa.2023.107770.

[117] Martinez, P., & Nutt, S. (2024). Resistance Welding of Carbon Fiber Reinforced Vitrimer Composites. *Composites Part X (MDPI)*, 8(12), 498. https://doi.org/10.3390/jcs8120498.

[118] Kim, G., Caglayan, C., & Yun, G. J. (2022). Epoxy-Based Catalyst-Free Self-Healing Elastomers at Room Temperature Employing Aromatic Disulfide and Hydrogen Bonds. *ACS Omega*, *7*(49), 44750–44761. https://doi.org/10.1021/acsomega.2c04559.

[119] Luo, J., Wang, T., Sim, C., & Li, Y. (2022). Mini-Review of Self-Healing Mechanism and Formulation Optimization of Polyurea Coating. *Polymers*, *14*(14), 2808. https://doi.org/10.3390/polym14142808.

[120] Si, H., Zhou, L., Wu, Y., Song, L., Kang, M., Zhao, X., & Chen, M. (2020). Rapidly reprocessable, degradable epoxy vitrimer and recyclable carbon fiber reinforced thermoset composites relied on high contents of exchangeable aromatic disulfide crosslinks. *Composites Part B: Engineering*, 199, 108278. https://doi.org/10.1016/j.compositesb.2020.108278.

[121] Markaide, N., Aretxabaleta, L., Zornoza, A., Arrieta, S., & Aizpurua, J. (2022). Study into the Mechanical Properties of a New Aeronautic-Grade Epoxy-Based Carbon-Fiber-Reinforced Vitrimer. *Polymers*, 14(7), 1223. https://doi.org/10.3390/polym14061223.

[122] Perrin, H., Berthomier, K., Mark, C., Motta, N., & Mohanty, G. (2022). Reversing fatigue in carbon-fiber reinforced vitrimer composites. *Carbon*, 187, 140–148. https://doi.org/10.1016/j.carbon.2021.10.077.

[123] Perrin, H., Vaudemont, R., Del Frari, D., Verge, P., Puchot, L., & Bodaghi, M. (2024). On the cyclic delamination-healing capacity of vitrimer-based composite laminates. *Composites Part A: Applied Science and Manufacturing*, 177, 107935. https://doi.org/10.1016/j.compositesa.2023.107935.

[124] Sharma, H., Rana, S., Singh, P., Hayashi, M., Binder, W. H., Rossegger, E., Kumar, A., & Schlögl, S. (2022). Self-healable fiber-reinforced vitrimer composites: overview and future prospects. *RSC Advances*, 12(50), 32569–32582. https://doi.org/10.1039/D2RA05103F.

[125] Guo, X., Liu, F., Lv, M., Chen, F., Gao, F., Xiong, Z., Chen, X., Shen, L., Lin, F., & Gao, X. (2022). Self-Healable Covalently Adaptable Networks Based on Disulfide Exchange. *Polymers*, *14*(19), 3953. https://doi.org/10.3390/polym14193953.

[126] Canadell, J., Goossens, H., & Klumperman, B. (2011). Self-Healing Materials Based on Disulfide Links. *Macromolecules*, *44*(8), 2536–2541. https://doi.org/10.1021/ma2001492.

[127] Cremlyn, R. J. W. (1996). *An introduction to organosulfur chemistry*. Wiley.

[128] Matxain, J. M., Asua, J. M., & Ruipérez, F. (2016). Design of new disulfide-based organic compounds for the improvement of self-healing materials. *Physical Chemistry Chemical Physics*, *18*(3), 1758–1770. https://doi.org/10.1039/C5CP06660C.

[129] Nevejans, S., Ballard, N., Miranda, J., Reck, B., & Asua, J. M. (2016). The underlying mechanisms for self-healing of poly(disulfide)s. *Phys. Chem. Chem. Phys.*, *18*. https://doi.org/10.1039/C6CP04028D.

[130] *4,4'-Dithiodianiline*. (n.d.). Retrieved April 12, 2026, from https://www.chemspider.com/Chemical-Structure.12344.html.

[131] Kuhzadmohammadi, A., & Zhang, N. (2025). Atomistic modeling of bond exchange reaction and self-healing mechanisms in epoxy vitrimers. *European Polymer Journal*, *239*, 114273. https://doi.org/10.1016/j.eurpolymj.2025.114273.

[132] Shundo, A., Yamamoto, S., & Tanaka, K. (2022). Network Formation and Physical Properties of Epoxy Resins for Future Practical Applications. *JACS Au*, *2*(7), 1522–1542. https://doi.org/10.1021/jacsau.2c00120.

[133] Jin, F.-L., Li, X., & Park, S.-J. (2015). Synthesis and application of epoxy resins: A review. *Journal of Industrial and Engineering Chemistry*, *29*, 1–11. https://doi.org/10.1016/j.jiec.2015.03.026

[134] Moosburger-Will, J., Lachner, E., Löffler, M., Kunzmann, C., Greisel, M., Ruhland, K., & Horn, S. (2018). Adhesion of carbon fibers to amine hardened epoxy resin: Influence of ammonia plasma functionalization of carbon fibers. *Applied Surface Science*, *453*, 141–152. https://doi.org/10.1016/j.apsusc.2018.05.057.

[135] Lin, J., Sun, C., Min, J., Wan, H., & Wang, S. (2020). Effect of atmospheric pressure plasma treatment on surface physicochemical properties of carbon fiber reinforced polymer and its

interfacial bonding strength with adhesive. *Composites Part B: Engineering*, *199*, 108237. https://doi.org/10.1016/j.compositesb.2020.108237

[136] Xiao, J., Zhang, X., Zhao, Z., Liu, J., Chen, Q., & Wang, X. (2022). Rapid and Continuous Atmospheric Plasma Surface Modification of PAN-Based Carbon Fibers. *ACS Omega*, *7*(13), 10963–10969. https://doi.org/10.1021/acsomega.1c06818.

[137] Liu, Y., Zhan, Y., He, M., Xiao, C., Liu, S., Qin, S., & Yu, J. (2022). Amino-functionalized carbon fiber/polyamide 6 composites with enhanced interfacial and mechanical properties. *Journal of Materials Research and Technology*, *20*, 3229–3240. https://doi.org/10.1016/j.jmrt.2022.08.112.

[138] Pittman, C. U., Wu, Z., Jiang, W., He, G.-R., Wu, B., Li, W., & Gardner, S. D. (1997). Reactivities of amine functions grafted to carbon fiber surfaces by tetraethylenepentamine. Designing interfacial bonding. *Carbon*, *35*(7), 929–943. https://doi.org/10.1016/S0008-6223(97)00047-X.

[139] Benazzo, F., Sodano, H. A. (2022). Evaluation of Interfacial Shear Strength Healing Efficiency between Dynamic Covalent Bond-Based Epoxy and Functionalized Fiberglass. *ACS Applied Polymer Materials*, *(4)*(4). https://pubs.acs.org/doi/10.1021/acsapm.2c00215.

[140] Alaitz Ruiz de Luzuriaga, Nerea Markaide, Asier M. Salaberria, Itxaso Azcune1, Alaitz Rekondo, and, & Hans Jürgen Grande. (2022). *Aero Grade Epoxy Vitrimer towards Commercialization | MDPI*. Retrieved April 23, 2026, from https://www.mdpi.com/2073-4360/14/15/3180

[141] Van Lijsebetten, F., Spiesschaert, Y., Winne, J. M., & Du Prez, F. E. (2021). Reprocessing of Covalent Adaptable Polyamide Networks through Internal Catalysis and Ring-Size Effects.

Journal of the American Chemical Society, *143*(38), 15834–15844. https://doi.org/10.1021/jacs.1c07360

[142] Pepels, M., Filot, I., Klumperman, B., & Goossens, H. (2013). Self-healing systems based on disulfide–thiol exchange reactions. *Polymer Chemistry*, *4*(18), 4955–4965. https://doi.org/10.1039/C3PY00087G

[143] Chhetri, S., & Bougherara, H. (2021). A comprehensive review on surface modification of UHMWPE fiber and interfacial properties. *Composites Part A: Applied Science and Manufacturing*, *140*, 106146. https://doi.org/10.1016/j.compositesa.2020.106146.

[144] Marshall, S. J., Bayne, S. C., Baier, R., Tomsia, A. P., & Marshall, G. W. (2010). A review of adhesion science. *Dental Materials: Official Publication of the Academy of Dental Materials*, *26*(2), e11-16. https://doi.org/10.1016/j.dental.2009.11.157.

[145] Primc, G., & Mozetič, M. (2024). Surface Modification of Polymers by Plasma Treatment for Appropriate Adhesion of Coatings. *Materials*, *17*(7), 1494. https://doi.org/10.3390/ma17071494.

[146] Mohammadi, M., Ishak, M. R., & Sultan, M. T. H. (2024). Exploring Chemical and Physical Advancements in Surface Modification Techniques of Natural Fiber Reinforced Composite: A Comprehensive Review. *Journal of Natural Fibers*, *21*(1), 2408633. https://doi.org/10.1080/15440478.2024.2408633.

[147] Veiga, A. T. V., da Silva, Y. F., Cavalcante, R. C., & Simão, R. A. (2025). SF6 Plasma Surface Modification of Flax Fibers for Improved Adhesion in Polypropylene Composites. *Fibers and Polymers*, *26*(6), 2569–2579. https://doi.org/10.1007/s12221-025-00949-6.

[148] Sasmazel, T. H., Alazzawi, M., & Kadim Abid Alsahib, N. (2021). Atmospheric Pressure Plasma Surface Treatment of Polymers and Influence on Cell Cultivation. *Molecules*, *26*(6), 1665. https://doi.org/10.3390/molecules26061665.

[149] Hegemann, D., Hanselmann B., Blanchard, N., & Amberg, M. (2014). Plasma-Substrate Interaction during Plasma Deposition on Polymers. *Contributions to Plasma Physics, (54)*(2). https://doi.org/10.1002/ctpp.201310064.

[150] Donnet, J. B., Brendle, M., Dhami, T. L., & Bahl, O. P. (1986). Plasma treatment effect on the surface energy of carbon and carbon fibers. *Carbon*, *24*(6), 757–770. https://doi.org/10.1016/0008-6223(86)90186-7.

[151] Blackman, B. R. K., Kinloch, A. J., & Watts, J. F. (1994). The plasma treatment of thermoplastic fibre composites for adhesive bonding. *Composites, The Challenge of Composites*, *25*(5), 332–341. https://doi.org/10.1016/S0010-4361(94)80003-0.

[152] Mandal, T., Ghanbarian, M., Ozten, U., & Naraghi, M. (2025). Unravel the nature of interface bonding and self-healing in vitrimer-carbon fiber composites. *Composites Part A: Applied Science and Manufacturing*, *199*, 109253. https://doi.org/10.1016/j.compositesa.2025.109253.

[153] Shi, Q., Jin, C., Chen, Z., An, L., & Wang, T. (2023). On the Welding of Vitrimers: Chemistry, Mechanics and Applications. *Advanced Functional Materials*, *33*(36), 2300288. https://doi.org/10.1002/adfm.202300288.

[154] Dominguez-Lopez, I., Domínguez-Díaz, M., García-García, A. L., Barceinas-Sánchez, J. D. O., & Martínez, H. (2021). Effect of atmospheric plasma treatment on the wettability of UHMWPE. *Materials Letters*, *285*, 129159. https://doi.org/10.1016/j.matlet.2020.129159.

[155] Rekondo, A., Martin, R., Luzuriaga, A. R. de, Cabañero, G., Grande, H. J., & Odriozola, I. (2014). Catalyst-free room-temperature self-healing elastomers based on aromatic disulfide metathesis. *Materials Horizons*, *1*(2), 237–240. https://doi.org/10.1039/C3MH00061C.

[156] Vrekhem, S. V., Vloebergh, K., Asadian, M., Vercruysse, C., Declercq, H., Van Tongel, A., De Wilde, L., De Geyter, N., & Morent, R. (2018). Improving the surface properties of an UHMWPE shoulder implant with an atmospheric pressure plasma jet. *Scientific Reports*, 8:4720. https://www.nature.com/articles/s41598-018-22921-6.

[157] Zaldivar, R. J., Kim, H. I., Steckel, G. L., Nokes, J. P., & Morgan, B. A. (2010). Effect of Processing Parameter Changes on the Adhesion of Plasma-treated Carbon Fiber Reinforced Epoxy Composites. *Journal of Composite Materials*, *44*(12), 1435–1453. https://doi.org/10.1177/0021998309355846.

[158] Lorenz, N., Zawadzki, T., Keller, L., Fuchs, J., Fischer, K., & Hopmann, Ch. (2024). Characterization and modeling of an epoxy vitrimer based on disulfide exchange for wet filament winding applications. *Polymer Engineering & Science*, *64*(8), 3682–3702. https://doi.org/10.1002/pen.26805.

[159] V. Švorčík, K. Kolářová, P. Slepička, A. Macková, M. Novotná, and V. Hnatowicz, "Modification of surface properties of high and low density polyethylene by Ar plasma discharge," *Polymer Degradation and Stability*, vol. 91, pp. 1219–1225, 2006.

[160] J. Hubert, T. Dufour, N. Vandencasteele, S. Desbief, R. Lazzaroni, and F. Reniers, "Understanding polyethylene surface functionalization by an atmospheric He/O_2 plasma through combined experiments and simulations," *Journal of Physics D: Applied Physics*, vol. 47, 485203, 2014. Preprint available: https://arxiv.org/pdf/1605.09724.

[161] S. Abou Rich, T. Dufour, P. Leroy, L. Nittler, J.-J. Pireaux, and F. Reniers, "LDPE films treated by an atmospheric Ar–O_2 post-discharge: functionalization, etching, degradation and partial recovery of the native wettability state," *Journal of Physics D: Applied Physics*, vol. 47, 065203, 2014. Preprint available: https://arxiv.org/pdf/1604.08753.

[162] B. C. Smith, "The Infrared Spectra of Polymers II: Polyethylene," *Spectroscopy*, vol. 36, no. 9, pp. 24–29, 2021. Available: https://www.spectroscopyonline.com/view/the-infrared-spectra-of-polymers-ii-polyethylene.

[163] G. Bredács et al., "Prediction of polyethylene density from FTIR and Raman spectroscopy using multivariate data analysis," *Polymer Testing*, vol. 104, 107406, 2021. DOI: 10.1016/j.polymertesting.2021.107406.

[164] B. C. Smith, "How to Properly Compare Spectra, and Determining Alkane Chain Length From Infrared Spectra," *Spectroscopy*, 2022. Available: https://www.spectroscopyonline.com/view/how-properly-compare-spectra-and-determining-alkane-chain-length-infrared-spectra.

[165] M. Lehocký, H. Drnovská, B. Lapčíková, A. M. Barros-Timmons, T. Trindade, M. Zembala, and L. Lapčík, "Plasma surface modification of polyethylene," *Colloids and Surfaces A: Physicochemical and Engineering Aspects*, vol. 222, no. 1–3, pp. 125–131, 2003. DOI: 10.1016/S0927-7757(03)00242-5.

[166] R. R. Deshmukh and A. R. Shetty, "Surface characterization of plasma-modified polyethylene by contact angle experiments and ATR-FTIR spectroscopy," *Journal of Applied Polymer Science*, vol. 104, pp. 449–457, 2007.

[167] Fang, Z., Tu, Q., Shen, X., Yang, X., Liang, K., Pan, M., & Chen, Z. (2022). Biomimetic surface modification of UHMWPE fibers to enhance interfacial adhesion with rubber matrix via

constructing polydopamine functionalization platform and then depositing zinc oxide nanoparticles. *Surfaces and Interfaces*, *29*, 101728. https://doi.org/10.1016/j.surfin.2022.101728

[168] "Attenuated Total Reflectance (ATR)," Bruker Corporation. Available: https://www.bruker.com/en/products-and-solutions/infrared-and-raman/ft-ir-routine-spectrometer/what-is-ft-ir-spectroscopy/atr-attenuated-total-reflectance.html

[169] "Depth of penetration for ATR measurements," Specac Ltd. Available: https://specac.com/theory-articles/depth-of-penetration-for-atr-measurements-2/.

[170] G. Dent, "Contact and Orientation Effects in FT-IR ATR Spectra," *Spectroscopy*, 2016. Available: https://www.spectroscopyonline.com/view/contact-and-orientation-effects-ft-ir-atr-spectra.

[171] R. Morent, N. De Geyter, C. Leys, L. Gengembre, and E. Payen, "Comparison between XPS- and FTIR-analysis of plasma-treated polypropylene film surfaces," *Surface and Interface Analysis*, vol. 40, pp. 597–600, 2008. DOI: 10.1002/sia.2619.

[172] S.-C. Shi and T.-W. Chang, "FTIR study of the surface properties and tribological behaviors of plasma-modified UHMWPE and zirconia," *Optical and Quantum Electronics*, vol. 50, 440, 2018. DOI: 10.1007/s11082-018-1694-7.

[173] Desimoni, E., Casella, G. I., Morone, A., & Salvi, A. M. (1990). XPS determination of oxygen-containing functional groups on carbon-fibre surfaces and the cleaning of these surfaces. *Surface and Interface Analysis*, *15*(10), 627–634. https://doi.org/10.1002/sia.740151011

[174] Immergut, E. H., & Mark, H. F. (1965). Principles of Plasticization. In *Plasticization and Plasticizer Processes* (Vol. 48, pp. 1–26). AMERICAN CHEMICAL SOCIETY. https://doi.org/10.1021/ba-1965-0048.ch001

[175] Faruk, O., Bledzki, A. K., Fink, H.-P., & Sain, M. (2012). Biocomposites reinforced with natural fibers: 2000–2010. *Progress in Polymer Science, Topical Issue on Polymeric Biomaterials*, *37*(11), 1552–1596. https://doi.org/10.1016/j.progpolymsci.2012.04.003.

[176] Kamarudin, S. H., Mohd Basri, M. S., Rayung, M., Abu, F., Ahmad, S., Norizan, M. N., Osman, S., Sarifuddin, N., Desa, M. S. Z. M., Abdullah, U. H., Mohamed Amin Tawakkal, I. S., & Abdullah, L. C. (2022). A Review on Natural Fiber Reinforced Polymer Composites (NFRPC) for Sustainable Industrial Applications. *Polymers*, *14*(17), 3698. https://doi.org/10.3390/polym14173698.

[177] AhmadvashAghbash, S., Verpoest, I., Swolfs, Y., & Mehdikhani, M. (2023). Methods and models for fibre–matrix interface characterisation in fibre-reinforced polymers: A review. *International Materials Reviews*, *68*(8), 1245–1319. https://doi.org/10.1080/09506608.2023.2265701

VITA

Chase McCullar is a Mechanical Engineering Master of Science student at the University of Tennessee, Knoxville. He was born and raised in Knoxville, Tennessee. Chase completed his Bachelor of Science in Mechanical Engineering at the University of Tennessee, Knoxville in 2024. After graduation, Chase will be working at Y-12 as a Tooling Design Engineer. In his free time, Chase likes to play golf, read science fiction books, and work with the 4th graders at his church.